

Structure of the human ATM kinase and mechanism of Nbs1 binding

C. Warren¹, N.P. Pavletich^{1,2,*}

Affiliations:

¹ Structural Biology Program, Memorial Sloan Kettering Cancer Center, New York, NY, USA.

² Howard Hughes Medical Institute, Memorial Sloan Kettering Cancer Center, New York, NY, USA.

* Correspondence to: PavletiN@mskcc.org

Abstract

DNA double-strand breaks (DSBs) can lead to mutations, chromosomal rearrangements, genome instability, and cancer. Central to the sensing of DSBs is the ATM (Ataxia-telangiectasia mutated) kinase, which belongs to the phosphatidylinositol 3-kinase-related protein kinase (PIKK) family. In response to DSBs, ATM is activated by the MRN (Mre11-Rad50-Nbs1) protein complex through a poorly-understood process that also requires double-stranded DNA. Previous studies indicate that the FxF/Y motif of Nbs1 directly binds to ATM, and is required to retain active ATM at sites of DNA damage. Here we report the 2.5 Å resolution cryo-EM structures of human ATM and its complex with the Nbs1 FxF/Y motif. In keeping with previous structures of ATM and its yeast homolog Tel1, the dimeric human ATM kinase adopts a symmetric, butterfly-shaped structure. The conformation of the ATM kinase domain is most similar to the inactive states of other PIKKs, suggesting that activation may involve an analogous realigning the N and C lobes along with relieving the blockage of the substrate-binding site. We also show that the Nbs1 FxF/Y motif binds to a conserved hydrophobic cleft within the Spiral domain of ATM, suggesting an allosteric mechanism of activation. We evaluate the importance of these structural findings with mutagenesis and biochemical assays.

Introduction

Ataxia-telangiectasia mutated (ATM) is a large protein kinase with a central role in the cellular response to DNA double-strand breaks (DSBs) and related genotoxic stress¹. Mutations in ATM are responsible for Ataxia-telangiectasia (AT), which is a rare, autosomal recessive disorder characterized by cerebellar degeneration, immunodeficiency, sensitivity to radiation and cancer susceptibility².

ATM, which belongs to the phosphatidylinositol 3 kinase-like protein kinase (PIKK) family², is essential for the sensing of DSBs during the cell cycle. It functions in association with the MRN protein complex consisting of the Mre11, Rad50 and Nbs1 proteins³. MRN contributes to the localization of ATM to DSBs, and together with double-stranded DNA (dsDNA), it activates ATM as a protein kinase. ATM then phosphorylates a wide range of downstream effector proteins, such as p53, Chk2, Brca2, and H2A.X, leading to the activation of cell cycle checkpoints and homology-directed repair (HDR)^{4–6,7–9}. Mutations in all three members of the MRN complex cause disorders that are phenotypically similar to AT^{10–12}.

The MRN complex rapidly associates with DNA ends upon DSB formation, and it is a known component of ionizing radiation-induced foci (IRIF)^{13,14}. The Mre11 subunit has endonuclease and exonuclease activities that are implicated in DNA end processing^{15,16}, although nuclease-inactive mutants in yeast have only mild defects in responding to ionizing radiation (IR)¹⁷. Rad50 is a member of the structural maintenance of chromatin (SMC) family of proteins. It contains an ATPase domain, a long antiparallel coiled coil, and a zinc hook domain that is thought to tether multiple MRN complexes^{18–20}. Nbs1 contains N-terminal FHA and BRCT domains that are required for association with phosphorylated

proteins such as H2A.X, CtBP-interacting protein (CtIP), and mediator of DNA damage checkpoint protein 1 (Mdc1) at IRIF^{21,22}. While the C-terminal half of Nbs1 is largely disordered²³ it contains short sequence motifs for binding to Mre11 and ATM^{24,25}.

The activation of ATM by MRN is incompletely understood. The yeast homolog of ATM, Tel1, can associate with each of the individual subunits of the corresponding Mre11-Rad50-Xrs2 complex²⁶. In the yeast system, Xrs2 is required for Tel1 recruitment to DSBs *in vivo*^{27,28}, but *in vitro* Tel1 activation appears more dependent on Rad50, as either Rad50-Mre11 or Rad50-Xrs2 but not Mre11-Xrs2 can partially activate Tel1 in the presence of DNA²⁶. The ATM-binding segment of Nbs1 has been mapped to a sequence motif termed FxF/Y (residues 740-749) at the C-terminus²⁵. Those of Mre11 and Rad50 have not yet been identified. The Nbs1 FxF/Y motif is necessary for ATM recruitment to MRN-bound DSBs and for ATM activation in *Xenopus* extracts²⁵ and human cell lines²⁹. However, FxF/Y deletion affects only a subset of the checkpoint functions, with non-uniform effects on downstream substrate phosphorylation²⁹. In addition, fibroblasts from mice harboring an Nbs1 C-terminal deletion (Nbs1^{ΔC/ΔC}) do not display overt sensitivity to IR, although they exhibit defective intra-S phase checkpoint activation, apoptosis induction, and phosphorylation of a subset of ATM targets³⁰. Taken together, these results suggest that the ATM-Nbs1 interaction is not strictly required to initiate ATM activation, but it is likely necessary to stabilize activated ATM at sites of DNA damage and is critical for certain ATM-mediated checkpoint functions. This may reflect the ability of the remaining MRN subunits to also interact with ATM, or additional factors within IRIFs may aid in the recruitment of ATM *in vivo* to partially compensate for the loss of the Nbs1 C-terminus.

Along with ATM, the PIKK family also includes ATR, DNA-PKcs, mTOR, SMG1, and TRRAP³¹. These mammalian PIKKs coordinate diverse cellular processes, with ATR involved in the response to collapsed replication forks, DNA-PKcs in non-homologous end joining (NHEJ), mTOR in metabolism and cellular homeostasis, SMG1 in nonsense-mediated mRNA decay, and the catalytically inactive TRRAP in scaffolding chromatin remodeling complexes^{32,33}. Like ATM, these PIKK kinases are switched on by binding to their cognate activating proteins or protein complexes. The PIKKs share sequence homology across their C-terminal portion that consists of the ~700-residue FAT domain (residues 1899-2613 of ATM) and subsequent ~400-residue kinase domain (KD; residues 2614-3056 of ATM). Their N-terminal regions are divergent, and they adopt α - α solenoid structures typically consisting of two or more helical-repeat domains.

The cryo-EM structure of human ATM, based on a reconstruction of 4.4 Å to 5.7 Å resolution, showed that it forms a dimer through interactions between the FAT domains and also between the FAT and kinase domains³⁴. The FAT-KD interactions involve a region of the KD, termed the PRD (PIKK Regulatory Domain), that sequesters the putative polypeptide substrate-binding site³⁵, as deduced from comparisons to canonical protein kinases³⁶. This arrangement was thus suggested to maintain ATM in an inactive state by inhibiting substrate binding³⁴. The N-terminal α - α solenoids are uninvolved in dimerization³⁴. A subsequent cryo-EM analysis reported a monomeric form at 7.8 Å resolution, in addition to the canonical dimer at 4.3 Å³⁷. The Tel1 homolog has been amenable to higher resolution structure determination³⁸, with recent structures of the *Chaetomium thermophilum* and *Sacharomyces cerevisiae* Tel1 reported at overall resolutions of 3.7 Å and 3.9 Å, respectively^{39,40}. These Tel1 structures exhibited similar

dimerization interfaces as ATM, including the region that blocks part of the putative substrate-binding site. Based on the higher resolutions of the Tel1 reconstructions, it was suggested that the kinase active site residues are in a catalytically competent organization, with the implication that the inaccessibility of the substrate-binding site is the primary mechanism of keeping ATM inactive. While Tel1 and ATM share a similar structural organization, the N-terminal ~1800 residues preceding the FAT domain do not have detectable sequence homology.

Here we report the cryo-EM structure of human ATM as well as the structure of ATM bound to a peptide containing the Nbs1 FxF/Y motif, both at an overall resolution of 2.5 Å. The organization of residues in the ATM catalytic cleft are very similar to those of the inactive states of mTOR and DNA-PKcs, the two PIKKs for which high-resolution structures have been reported for both the inactive and active states^{41–46}. Notably, ATM does not exhibit the conformational change that is characteristic of the active states of mTOR and DNA-PKcs kinase domains^{42,44}. Together with biochemical data, this suggests that activation of ATM by MRN may involve a conformational change that, in addition to relieving the partial blockage of the substrate-binding site, also realigns catalytic residues.

Results

Structure of the human ATM dimer

Daniel L. Yocum

FLAG-tagged ATM was purified from a stably-transfected cell line (Figure 1—figure supplement 1A). This preparation displays low but measurable kinase activity towards a p53 substrate peptide (Figure 1—figure supplement 1B). Cryo-EM samples were prepared

by mixing ATM with the non-hydrolyzable ATP analog adenylyl-imidodiphosphate (AMP-PNP) and MgCl_2 . The cryo-EM data yielded a consensus reconstruction in point group C2 that extended to an overall resolution of 2.5 Å as determined from gold standard Fourier shell correlation (FSC = 0.143) (Supplementary File 1, Figure 1—figure supplement 2). Subsequently, partial signal subtraction followed by symmetry expansion and focused refinement was used to improve the density of the N-terminal α - α solenoid regions (see Methods and Figure 1—figure supplement 3)⁴⁷. The focused reconstructions show clear density for the majority of the side chains, allowing for the mapping of conserved residues and cancer-associated missense mutations (Figure 1—figure supplements 3 to 7). The refined model contains over 90 % of the ATM residues, with the remaining residues in poorly-ordered or disordered loops. While this manuscript was being prepared, a cryo-EM structure of ATM bound to the inhibitor KU-55933 was reported at an overall resolution of 2.8 Å⁴⁸. Our structure of ATM bound to AMP-PNP is highly similar with a root mean square deviation (RMSD) of 0.9 Å based on 2453 aligned C α atoms.

In keeping with previous structures of ATM and Tel1^{34,38,39,40,49}, ATM adopts a butterfly shaped dimer with the FAT and KD domains (hereafter FATKD) forming a dimeric body and the N-terminal α - α solenoids of ~1,900 residues, previously described as Spiral and Pincer^{34,49}, extending away from this body. In our structure (Figure 1A to C), the Spiral domain extends across residues 1 to 1166, the Pincer domain across residues 1167 to 1898, the FAT domain (named after FRAP, ATM, TRRAP) across residues 1899 to 2613, and the Kinase domain across residues 2614 to 3056. As described for other PIKKs^{41,42}, the Kinase domain consists of an N-terminal lobe (N lobe, residues 2614-2770) and a C-terminal lobe (C lobe, residues 2771-2957), with the catalytic cleft in between the two. The

C lobe ends with the FAT C-terminal domain (FATC, residues 3027-3056) that is characteristic of the PIKK family and is absent from canonical kinases^{41,42}.

The N-terminal Spiral and Pincer domains, which consists mostly of HEAT repeats, are mobile relative to the FATKD dimer body. 3D classification indicated that the Spiral and Pincer domains have no preferred conformation relative to the FATKD body (Figure 1—figure supplement 2C). The most “open” and “closed” subclasses were each refined to an overall resolution of 2.8 Å as determined from the gold standard FSC (Figure 1—figure supplement 2C and D, Video 1). In the most open conformation, the N-terminal tips of the Spiral domains are separated by ~134 Å, while these same regions are separated by ~125 Å in the most closed conformation (Figure 1—figure supplement 6A to D). The mobility originates in part from flexibility within the Pincer domain, which forms the elbow-like structure of the α -solenoid arm that extends from the N-terminus to the start of the FAT domain. This flexibility is associated with the solenoid arm adopting a continuum of positions relative to the FATKD. Similar, albeit more extensive flexibility has also been observed with the cryo-EM reconstruction of *C. thermophilum* Tel1³⁹. The flexibility of the Spiral and Pincer domains does not lead to any significant conformational changes in the FATKD segment, which can be superimposed with a 0.39 Å root mean square deviation (r.m.s.d.) in the positions of 1,048 C α atoms from the open and closed conformation structures (Figure 1—figure supplement 6E and F). Therefore, it is unlikely that any of these subclasses represent an intrinsically more active conformation of the ATM dimer.

The ATM FAT domain plays a central role in dimerization, which buries ~3,800 Å² of surface area on each ATM protomer (Figure 1—figure supplement 7)⁵⁰. As with other PIKKs, the FAT domain consists of three Tetratricopeptide Repeat Domain subdomains

(TRD1 residues 1899-2025, TRD2 residues 2026-2192, and TRD3 residues 2193-2479) followed by a HEAT-repeat subdomain (HRD residues 2480-2613) (Figure 2A). It adopts a “C”-shaped structure that partially encircles the KD. In an arrangement that has been described as a C-clamp⁴¹, TRD1 packs with the KD C lobe, while the HRD packs with both N and C lobes adjacent to the catalytic cleft (Figure 2B). This arrangement is conserved among structurally characterized PIKKs^{31,33}. TRD1 additionally packs with multiple regions of the Pincer domain that precedes it. Ser1981, a conserved TRD1 residue whose autophosphorylation coincides with ATM activation^{51,52}, is in a 9-residue disordered loop between the α 1c and α 1d α helices (prefix “f” denotes FAT domain helices) and is not visible in our map. However, due to the limited length of this loop and its position relative to the active site, it is unlikely that Ser1981 would be phosphorylated by either protomer in the dimeric structure. This suggests that Ser1981 is either phosphorylated by a separate ATM molecule during activation, or that a major MRN-DNA induced structural rearrangement precedes Ser1981 autophosphorylation in the activation pathway.

TRD2, which is composed of 9 α helices (α 4 to α 12), forms a substantial part of the dimer interface, with two separate regions contributing roughly one-third of the surface area buried on dimerization ($\sim 1,350 \text{ \AA}^2$ of TRD2 buried per ATM protomer) (Figure 2C). TRD2 helices α 5 to α 8 contact the corresponding TRD2 region of the second protomer in a 2-fold symmetric interface (Figure 2D), while helices α 4 to α 5 contact TRD3 helices α 16 to α 18. The majority of these intermolecular interactions are van der Waals contacts by hydrophobic residues, along with a small hydrogen bond network and electrostatic interactions at the periphery of the hydrophobic residues. Additional buried intermolecular

salt bridges between highly conserved residues Arg2032-Glu2272 and Lys2044-Glu2304 likely function to further stabilize the dimer interface.

TRD3, which is composed of 10 α helices (α 13 to α 22), accounts for the largest number of dimerization contacts and for slightly over half the surface area buried. In addition to the aforementioned TRD3-TRD2 intermolecular contacts, TRD3 also contacts the kinase domain of the second protomer. These contacts, which account for approximately one-quarter ($\sim 930 \text{ \AA}^2$) of the surface area buried on dimerization, involve a C lobe surface patch that extends to the edge of the catalytic cleft (Figure 2E and F). The most prominent interactions are made by the TRD3 α 21- α 22 helices, which form a long coiled coil that extends across the dimer interface and packs with the C lobe near the catalytic cleft. These contacts are centered on the C lobe α 9b helix (prefix “k” denotes kinase domain helices) that is part of the PRD (Figure 2E). As reported previously^{34,38–40}, the α 9b helix occludes part of the putative substrate-binding site, and the packing of the coiled coil against it may well stabilize this autoinhibitory conformation. A second set of contacts, made by the TRD3 helices α 19 to α 20, are centered on the FATC α 11 helix located at the end of the C lobe patch, distal from the catalytic cleft (Figure 2F). The FAT domain thus appears to serve multiple functions: it clamps down on the KD N and C lobes in an arrangement thought to be critical in stabilizing the inactive KD conformation of other PIKKs⁴¹, it is critical for the dimerization of ATM, and it may help stabilize the α 9b conformation that occludes the putative substrate-binding site of the other protomer.

Kinase domain conformation

The binding of the AMP-PNP cofactor to the catalytic cleft is overall similar to those of other PIKKs^{34,35,41,42} (Figure 3A to C). The adenine ring is sandwiched between hydrophobic or aromatic residues from the N lobe (Leu2715, Leu2767 and Trp2769) and C lobe (Leu2877 and Ile2889), while the N6 and N1 groups hydrogen bond to backbone carbonyl and amide groups of Glu2768 and Cys2770, respectively (Figure 3B and C). While the involvement of these residues is conserved among PIKKs, the precise position and orientation of the purine group relative to the C lobe exhibits some variation (up to ~1.5 Å and ~20°) among PIKK structures^{35,42}. Similarly, the conformations of the AMP-PNP ribose and phosphate groups in the ATM structure are within the range of variability among PIKK structures, albeit a wider range than that of the purine group. This is possibly due to the use of different ATP analogs, and in the case of mTOR due to conformational change between the inactive and active states⁴².

The phosphate groups interact with the N lobe directly, through a contact between Lys2717 and the α phosphate group, and with the C lobe indirectly, through the Mg^{2+} cofactor. The position of Lys2717 is equivalent to a critical lysine residue in canonical kinases, where it is thought to orient the γ phosphate group for phosphotransfer^{41,53}. Whether the lysine residue has an analogous role in PIKKs is not yet known. In addition to this lysine residue, canonical kinases have an N lobe β hairpin, rich in glycine residues, that packs against the phosphate groups when both the ATP and peptide substrates are assembled⁵³. The corresponding region in PIKKs is more variable in sequence. In ATM, it contains Gly2694 and Gly2695, with the latter's backbone amide being ~4 Å away from the β phosphate group. This glycine-rich loop also contains Val2696 and Asn2697 that, together with Tyr2969 on $\kappa 9b$, appear to occlude the γ phosphate (Figure 3D). The Mg^{2+}

ion, which contacts the AMP-PNP α phosphate group, is coordinated by Asn2875 and Asp2889 of the C lobe – interactions conserved among both PIKKs and canonical protein kinases^{31,38–41}. Our maps show only a low level of density for a second Mg^{2+} ion thought to be involved in phosphoryl transfer by canonical kinases^{54,55}. The second Mg is often poorly ordered in canonical kinases as well as PIKKs^{38–40}.

On the C lobe, the magnesium ligands and other critical catalytic residues map to two loops, named catalytic loop (residues 2866 to 2875) and activation loop (residues 2888 to 2911) by analogy to canonical kinases⁴¹. As with previous studies of ATM and Tel1, these loops are well ordered and their catalytic residues show clear density in our maps. The catalytic loop contains Asp2870, Asn2875 (a Mg^{2+} ligand) and His2872. Asp2870 acts as the catalytic base to deprotonate and likely orient the hydroxyl group of the incoming substrate⁵⁶ and His2872 is thought to stabilize the transition state of the phosphoryl transfer reaction⁴¹. The activation loop is named for its conformational change in the activation of canonical kinases, where it makes up part of the polypeptide substrate-binding site. Previous studies showed that the activation loop of ATM/Tel1 packs with the $k\alpha 9b$ helix of the PRD, and by analogy to canonical kinases it was suggested that the $k\alpha 9b$ helix may block substrate binding. This was recently confirmed by the cryo-EM analysis of the PIKK Smg1, which, like ATM, is specific for a glutamine residue in the position (P_{+1}) after the serine/threonine phosphorylation site. In the Smg1-UPF1 substrate structure³⁵, the glutamine side chain of the peptide substrate makes a pair of hydrogen bonds to backbone amide and carbonyl groups on the activation loop. This interaction is effectively mimicked in our ATM structure by the side chain of Gln2971 on the $k\alpha 9b$ helix of ATM (Figure 3—figure supplement 1).

It has been suggested that the Tel1/ATM active site residues are in a catalytically competent conformation, and thus the occlusion of the substrate-binding site would be the main mechanism of keeping the kinase autoinhibited^{34,38–40}. However, studies of mTOR have shown its activation involves a conformational change in the FAT domain, which in turn allows the KD N and C lobes to move relative to each other. This results in the realignment of catalytic residues on the N and C lobes relative to each other, bringing them into the correct register for efficient catalysis⁴². The recently reported active-state structure of DNA-PKcs recapitulates the N-C lobe conformational change on activation⁴⁴, raising the possibility that this is a common activation mechanism of PIKKs, irrespective of their distinct activators and N-terminal solenoid structures to which these activators bind.

Thus, to help evaluate whether the ATM active site residues are in a catalytically competent conformation, we superimposed the KD domains of ATM, mTOR and DNA-PKcs, the latter two in both their active and inactive conformations, by aligning their C lobe catalytic and activation loops. In this superposition (Figure 3F), the ATM N lobe is positioned remarkably similar to those of inactive mTOR and inactive DNA-PKcs, with the three N lobes forming a tightly clustered set clearly distinct from the cluster of active mTOR and active DNA-PKcs N lobes. The positions of the N lobe hairpin and other ATP-interacting residues relative to the C lobe catalytic and magnesium-coordinating residues are much closer to those of the inactive mTOR and DNA-PKcs structures compared the active ones (Figure 3G and H). This positioning thus suggests that in addition to relieving the blockage of the substrate-binding site, the activation of ATM may well involve a conformational change within the FAT domain and the associated change in the relative orientation of the N and C lobes of the kinase domain.

Structure of ATM bound to the C-terminus of Nbs1

Previous studies indicated that the Xrs2 C-terminal FxF/Y motif and the acidic region that immediately precedes it bind to two Tel1 regions spanning the Spiral and Pincer domains near the elbow^{25,40} (Figure 4A). As the Nbs1 C-terminal half is unstructured or loosely folded²³, we made cryo-EM grids using a 28-residue peptide (207 μ M) that encompasses the acidic region and FxF/Y motif of human Nbs1 (residues 727-754, hereafter referred to as Nc28) and human ATM (1.2 μ M).

The cryo-EM data yielded a consensus reconstruction in point group C2 that extended to 2.5 Å resolution as determined from the gold standard FSC (Figure 4—figure supplement 1). The initial map had additional density, absent in the apo ATM (Figure 4—figure supplement 1D), at the ATM Spiral domain. Partial signal subtraction and symmetry expansion procedures followed by iterative focused 3D classifications identified 75 % of the particles that had the extra density (481,066 particles; Figure 1—figure supplement 3A and Figure 4—figure supplement 1C). After focused refinements of the ATM Spiral domain, we built a 10-residue Nbs1 segment (⁷⁴⁰ADDLFRYNPY⁷⁴⁹) into the improved density guided by the unambiguous density of the side chains for Phe744 and Tyr746. According to local resolution estimation, the focused reconstruction has a resolution better than ~3.5 Å in the central portions of the peptide (Figure 4B, Figure 4—figure supplement 1G). There is no interpretable density for residues 727 to 739 preceding the built segment or residues 750 to 754 after. We note that in contrast to previous yeast two-hybrid assays indicating that the C-terminus of Xrs2 interacts with both the Spiral and Pincer domains of Tel1²⁵, we find no evidence of the ATM Pincer domain being involved in binding to the

302 Nbs1 peptide.

303 The Nbs1 peptide adopts an overall extended conformation except for one turn of a
304 3_{10} helix in the middle (residues Asp742 to Arg745; Figure 4C and D). It binds to a
305 hydrophobic groove between two helical repeats formed by helices $\alpha 39$ to $\alpha 42$ (denoted
306 “s” for Spiral domain helices). The most extensive ATM contacts are made by Nbs1
307 Leu743 and Phe744, which pack together preceding the 3_{10} helix. Phe744 inserts deepest
308 into the hydrophobic groove and makes van der Waals contacts to the side chains of
309 Ser978, Arg981, Cys987, Val1021, Ala1024, Phe1025, Leu1028, and Tyr1034 of ATM
310 (Figure 4C and D). Leu743, which is closer to the solvent exposed surface of the ATM
311 groove, packs with Ala1024, Leu1028 and His1027 (Figure 4C and D). Of the two acidic
312 residues that precede the Leu743-Phe744 pair, Asp741 hydrogen bonds with Ser978 and
313 Arg981, while Asp742 is solvent exposed and uninvolved in ATM contacts (Figure 4C and
314 D). Arg745, the last residue of the 3_{10} helix, has weaker side chain density, although its
315 guanidinium group is positioned between the side chains of Asn975 and Ser978 (Figure 4C
316 and D). Tyr746 is the last Nbs1 residue that contacts ATM. Its side chain, which is
317 stabilized by intramolecular stacking with Pro748, packs with side chain and backbone
318 groups of Gly1016, Gln1017 and Thr1020 of ATM (Figure 4C and D).

319 The ATM residues that make up the Nbs1 binding site, and in particular those at the
320 Leu743-Phe744 binding pocket, are highly conserved compared to the rest of Spiral
321 domain residues (Figure 1—figure supplement 4 and Figure 4—figure supplement 2A). In
322 addition, many of these ATM residues have been found mutated in cancer (Figure 1—
323 figure supplement 5D and E). Ser978 is a hotspot for cancer-associated missense
324 mutations and the structure suggests that the S978P mutation would disrupt the $\alpha 39$ helix

that forms part of the Nbs1-binding site, while S978A and S978Y would eliminate the interactions of Ser978 with Asp741 of Nbs1 (Figure 1—figure supplement 5D and E). Other cancer-associated missense mutations at the Nbs1 binding groove occur at lower frequencies. The structure suggests that the S974F mutation, in a region of limited solvent accessibility due to the Nc28 peptide, would likely cause a steric clash either with Arg745 of Nbs1 or other ATM backbone and side chain groups; R981C/H would eliminate the contact to Asp 741 of Nbs1; C987Y/W and F1025S/L, which map to a local hydrophobic core behind the α 39 and α 42 helices, would disrupt the structural integrity of the binding site of Nbs1 Phe744 and its vicinity. The abundance of mutations at the Nbs1 binding site suggest that the ATM-Nc28 interaction is functionally important for the ATM-mediated DNA damage response. Reported mutations in Nbs1 are fewer, but include the F744L mutation that would disrupt the most critical portion of the ATM-Nc28 interaction (Figure 1—figure supplement 5F).

The ATM structural elements at the Nbs1 binding site, including the hydrophobic pocket and adjacent cleft, are nearly identical in both the apo and Nc28-bound structures, indicating that Nc28 binding does not induce any noticeable structural rearrangements to this region (Figure 4—figure supplement 1D). Additionally, no significant changes to the structure of the kinase domain were observed when comparing the unbound and Nc28-bound states (Figure 4—figure supplement 2D). Consistent with these observations and with reports that ATM activation requires all 3 members of the MRN complex and dsDNA⁹, we observed no increase in ATM catalytic activity in steady-state kinase assays containing high concentrations of this peptide (Figure 4—figure supplement 2C). Finally, though previous studies suggest that the Nbs1 C-terminus may interact with the ATM FATC

domain^{38,57}, we observe no additional electron density within this region of ATM despite our sample containing a large molar excess of the Nc28 peptide.

The N-terminal acidic half of the peptide is not visible in our map. However, the orientation of the visible portion indicates that it likely extends into a basic patch created by ATM residues Arg981, Arg982, and Lys1033, raising the possibility that the acidic residue clusters (Glu728, Glu736 and Glu737) contribute to binding through long-range electrostatic interactions (Figure 4—figure supplement 2B). Alternatively, the acidic residues may engage in ATM interactions in the context of the intact MRN complex. Similarly, while the C-terminal 4 residues of Nbs1 (⁷⁵⁰LKRRR⁷⁵⁴) are also not visible, they would be in the vicinity of an acidic patch of ATM (Glu964, Asp965, Asp1007, Glu1009, and Asp1013; Figure 4—figure supplement 2B).

To evaluate the relative contributions of the ATM-Nbs1 contacts, we made several mutations in the FxF/Y motif and tested the ability of these mutant peptides to bind to ATM in a GST pull-down assay. Four mutations (F744A, R745A, Y746A, and ⁷⁴⁴FRY⁷⁴⁶ to ⁷⁴⁴AAA⁷⁴⁶) were introduced into a GST-tagged polypeptide corresponding to the C-terminal 147 residues of Nbs1 (GST-Nc147). While the wild-type GST-Nc147 and the R745A mutant both enriched for ATM in pull-down assays, all other mutations disrupted this interaction at least partially (Figure 4E). F744A and FRY to AAA mutations appeared to disrupt the interaction almost completely, whereas Y746A showed an intermediate effect. These results indicate that Nbs1 Phe744 is central to ATM binding, Tyr746 clearly contributes, while Arg745 makes at most a minor contribution in our assay.

The Mre11 binding motif of Nbs1 (residues 682-693) is located approximately 60 residues N-terminal to the FxF/Y motif, indicating that the MRN complex likely binds along

the Spiral and/or Pincer domains of ATM. Interestingly, we mapped multiple patches of conserved residues to the inner portion of the Spiral domain α -solenoid, which may represent binding sites for MRN-dsDNA or other effector proteins (Figure 1—figure supplement 7B). Notably, the Nbs1 interaction site is located over 100 Å away from the active site. This is reminiscent of mTOR and DNA-PKcs, whose activators, respectively Rheb and Ku-DNA, bind far from the KD and activate their respective kinases allosterically^{42,44}. This mechanism would suggest that the full MRN-dsDNA complex induces structural changes that are transmitted through the Spiral and Pincer domains to the FATKD, although the Rad50 coiled coil domain may be long enough to extend from the head of the MRN complex and make direct contacts to the KD and/or FATC to promote activation.

Biochemical analysis of MRN-mediated ATM activation and the role of the Nbs1 C-terminus

To better understand how human ATM kinase is activated and to further evaluate the role of the Nbs1 C-terminus, we expressed the human MRN complex in mammalian cells via transfection of a polycistronic vector (see Materials and Methods) and purified it to near homogeneity (Figure 5—figure supplement 1A). Each protein contains a C-terminal FLAG tag and Mre11 harbors the H129N mutation, which abolishes nuclease activity without interfering with DNA binding and ATM activation⁵⁸. We first evaluated the effect of increasing concentrations of the purified MRN complex on ATM activity using a substrate peptide from p53, whose phosphorylation by ATM activates the transcription program associated with the G1/S DNA-damage checkpoint. In keeping with findings with the Tel1-

MRX homologs²⁶, MRN alone stimulated the ATM kinase activity only modestly, by a factor of ~4 (Figure 5—figure supplement 1B). The half-maximal effective concentration (EC₅₀) of MRN was ~27 nM, indicative of a high affinity for ATM.

We next tested linear dsDNA fragments of lengths ranging from 100 to 2000 base pairs (bp) for their ability to stimulate ATM (25 nM) in the presence of MRN (250 nM; concentration ~10-fold above its EC₅₀ towards ATM alone). The dsDNA fragments were added at a constant base-pair concentration of 3.85 μ M (2.5 ng/ μ L of each fragment). dsDNA lengths greater than ~200 bp lead to maximal ATM activation, representing an additional ~25-fold increase in p53 phosphorylation relative to ATM-MRN alone, or a ~100-fold increase relative to ATM alone (Figure 5A, Figure 5—figure supplement 1H). This dsDNA length dependency for ATM-MRN activation is qualitatively similar to that reported for the Tel1-MRX complex²⁶. We then performed a dose response analysis for dsDNA of 100, 250 and 500 bps lengths. 250 and 500 bp dsDNA fragments stimulated with very similar EC₅₀ values of 1.8 nM and 1.5 nM, while stimulation by 100 bp dsDNA fragment was a factor of 5 lower compared to the maximal levels of the longer DNA fragments, even at the ~1000-fold higher concentration of 2.3 μ M (Figure 5B and Figure 5—figure supplement 1D). This suggests that the low-level activation of shorter dsDNA fragments is likely not due to their reduced affinity for ATM-MRN, and that structural aspects of longer DNA, such as the ability to span an extended binding site across the ATM dimer or to link distal binding sites on ATM-MRN, may be important. Stimulation by dsDNA is strictly dependent on the presence of the MRN complex, as in the absence of MRN, 350 bp dsDNA at a concentration of 25 nM, which is more than 10-fold above the EC₅₀ of the 250 and 500 bp DNA failed to activate (Figure 5—figure supplement 1E and H).

We next evaluated whether MRN-dsDNA affects the intrinsic catalytic step or peptide substrate binding. The steady state kinetic analysis of ATM phosphorylating the p53 substrate showed that MRN-dsDNA increased the catalytic step 460-fold, with k_{cat} values of 0.0005 s^{-1} and 0.24 s^{-1} in the absence and presence of MRN-DNA, respectively, while the K_{M} values were unchanged within experimental error ($58 \text{ }\mu\text{M}$ and $67 \text{ }\mu\text{M}$; Figure 5—figure supplement 1E and F). Time course assays performed under single-turnover conditions also indicate that MRN directly increases the rate of the catalytic step, as opposed to a hypothetically rate limiting product release step (Figure 5—figure supplement 1G).

We next made MRN containing the Nbs1 $^{744}\text{FRY}^{746}$ to $^{744}\text{AAA}^{746}$ mutation and titrated this mutant complex into kinase assays with saturating amounts of 350bp dsDNA present (Figure 5C). In contrast to pull-down assays, we observe only a minor defect in MRN-mediated activation of ATM kinase activity with this mutant. The maximal catalytic rate of ATM with this mutant was approximately 18 % lower compared to the wild-type MRN complex, although an effect on the EC_{50} of activation was not discernible. We note, however, that our *in vitro* assay conditions, such as the saturating dsDNA concentration, may not recapitulate the demonstrated requirement for MRN recruiting ATM to DNA *in vivo*^{27–29}.

Discussion

Our cryo-EM structure of human ATM shows an overall symmetric dimer, albeit with the Pincer and Spiral domains exhibiting some mobility arising from conformational flexibility within the Pincer domain. Nevertheless, this conformational flexibility does not

translate to any noticeable structural rearrangements within the FATKD segment, nor does it break the inherent symmetry of this segment (Figure 1—figure supplement 6). Previous cryo-EM studies of human ATM and yeast Tel1 have observed asymmetric dimers and monomers, the latter of which was shown to have increased catalytic activity^{34,37}. In our purifications and subsequent cryo-EM structure determination, we failed to find any particles representing asymmetric dimers or monomers, also consistent with the most recent cryo-EM structures of Tel1^{39,40}. While it is not clear how the asymmetric dimers and monomers arise, it is conceivable that expression and purification conditions may play a role. Detergents have previously been demonstrated to disrupt the ATM dimeric structure and increase ATM kinase activity independent of MRN⁵⁹. We note that the report of active monomer preparations demonstrated only an approximately 10-fold increase in catalytic activity relative to the inactive dimeric state³⁷, whereas our quantitative kinase assays show a ~100-fold activation upon MRN+long dsDNA addition (Figure 5—figure supplement 1H).

As noted in previous ATM and Tel1 structures^{34,38–40}, the apparent reason for the inhibited state of the ATM dimer is the $\kappa\alpha 9b$ helix packing against the putative substrate-binding site and inserting a glutamine side chain into the activation loop, at a site where a glutamine side chain from the substrate would bind (Figure 3—figure supplement 1)³⁵. As the $\kappa\alpha 9b$ helix packs with the TRD3 coiled coil of the other protomer in the dimer, an interaction that possibly stabilizes the $\kappa\alpha 9b$ conformation, the TRD3 coiled coil was proposed to couple ATM dimerization to autoinhibition^{34,38–40}.

The $\kappa\alpha 9b$ helix is part of the PRD domain, which was first described based on a yeast two-hybrid screen to identify the part of the ATR PIKK that interacts with its activator

463 TopBP1⁶⁰. The screen led to a minimal ATR fragment that encompasses $\kappa\alpha 9b$ and $\kappa\alpha 10$.
464 While scanning mutagenesis identified an ATR $\kappa\alpha 10$ residue that disrupts TopBP1-
465 mediated activation⁶⁰ it is not clear what role $\kappa\alpha 10$ plays in PIKK activation. The mutation
466 (K2589E) maps to a surface residue uninvolved in any interactions in the inactive ATR
467 structure⁶¹, and the corresponding ATM residue (Glu3007) is similarly surface-exposed
468 and devoid of any interactions. In addition, the $\kappa\alpha 10$ helix is an integral part of the PIKK C
469 lobe structure, and it is structurally invariant among inactive and active PIKK structures. It
470 is thus unlikely that $\kappa\alpha 10$ has a significant role in conformationally regulating the kinase. In
471 ATM, the $\kappa\alpha 9b$ and $\kappa\alpha 10$ helices are connected by 27-residue loop (residues 2975-3000)
472 that is not conserved across species and is not visible in our map (Figure 1—figure
473 supplement 4). An unstructured loop intervening the $\kappa\alpha 9b$ and $\kappa\alpha 10$ helices is present in
474 most PIKK structures reported to date, including a >1000 residue insertion in Smg1³⁵.

475 In structures of inactive DNA-PKcs, $\kappa\alpha 9b$ and subsequent $\kappa\alpha 9c$, a helix unique to
476 DNA-PKcs, also pack against the substrate-binding site and occlude it^{43,44}. However, even
477 though DNA-PKcs is glutamine directed as ATM, it does not have the equivalent of the
478 Gln2971-activation loop interaction of ATM. Nevertheless, upon DNA-PKcs activation, the
479 pair of $\kappa\alpha 9b$ and $\kappa\alpha 9c$ helices move to an alternate packing position on the C lobe and fully
480 expose the substrate-binding site⁴⁴. The movement of $\kappa\alpha 9b$ - $\kappa\alpha 9c$ is likely due entirely to
481 the realignment of the N and C lobes of DNA-PKcs, as this segment only interacts with the
482 kinase domain (DNA-PKcs does not have the equivalent of the ATM TRD3 coiled coil
483 packing with and possibly stabilizing $\kappa\alpha 9b$ across a dimer interface). By contrast, in
484 mTOR, which is not glutamine directed and instead prefers a hydrophobic residue at the
485 P₊₁ position, the $\kappa\alpha 9b$ helix does not block the putative substrate-binding site, nor does it

change conformation on activation⁴². Thus, while $\kappa\alpha 9b$ may play a role in the autoinhibition of ATM and a number of other PIKKs, this is not a conserved feature of the PIKK family.

Rather, several lines of evidence point to the realignment of the N and C lobes of the kinase domain as the key event in the activation of ATM. As discussed above, the relative orientation of the N and C lobes of ATM is remarkably similar to those of the inactive-state mTOR and DNA-PKcs structures, and distinct from those of the active-state counterparts, which cluster together (Figure 3F). The proper alignment of the N and C lobes is central to kinase activation, as residues critical for substrate binding and catalysis are distributed across the two lobes⁴².

The mechanism of a PIKK activation was initially established by comparing the inactive and active states of the mTOR holoenzyme⁴². That work pointed to the FAT domain being the key autoinhibitory element that keeps the N and C lobes and their active site residues in an unproductive configuration⁴². Binding of the mTOR activator, the small GTPase Rheb, causes a motion of the N-heat solenoid (comparable to the ATM Spiral in its location in the primary sequence but not in its structure). The motion of the N-heat solenoid pulls and twists the FAT domain on which it is anchored, causing it to undergo an extensive conformational change. This shifts the HRD of the FAT domain away from the N lobe, allowing the N lobe to relax to a productive configuration relative to the C lobe. The inhibitory effect of the FAT domain is supported by activating mTOR mutations, which map to residues that couple the N and C lobes and the FAT domain⁴².

The recent cryo-EM structures of activated DNA-PKcs recapitulate the FAT conformational change observed in mTOR⁴⁴. DNA-PKcs activation is triggered by the N-heat solenoid binding to the dsDNA end, stabilized by the Ku70-Ku80 complex. The Ku

complex interacts with DNA and the N- and M-heat DNA-PKcs domains, but it also utilizes two flexibly linked elements for additional contacts to DNA-PKcs. These may reflect an initial recruitment interaction, a role that the Nbs1 Nc28 peptide may also be involved in (Figure 4—figure supplement 2E). On DNA-end binding, the DNA-PKcs N-heat solenoid moves relative to M-heat. As with mTOR, N-heat is anchored on the FAT domain, and its motion allosterically induces a conformational change in the FAT domain that realigns the N and C lobes.

In both mTOR and DNA-PKcs, the N-heat solenoids that move are anchored on the FAT TRD2-TRD3 interface, at essentially the same location. And, even though their overall N-heat solenoids are structurally distinct, they both use a four-helix bundle followed by a loop to interact with their respective FAT domains. Our ATM structure reveals a remarkably similar interface between the FAT domain and the Pincer (equivalent to M-heat of mTOR and DNA-PKcs) from same protomer. The similarities include an identical TRD2-TRD3 site of the FAT domain and a four-helix bundle and loop element from the Pincer that binds to it, in essentially the same configuration as those of mTOR and DNA-PKcs (Figure 5—figure supplement 2A). Based on this structural conservation and the high level of FAT conservation across the PIKK family, it is conceivable that ATM activation also involves this same mechanistic step, with the activator MRN-dsDNA complex triggering the Pincer to pull on and twist the FAT domain to realign the N and C lobes (Figure 5—figure supplement 2B).

If movement of the Pincer domain is on the pathway of ATM activation, we presume dsDNA and MRN binding will involve portions of ATM beyond the Spiral that binds to Nc28 and which has been proposed to have site(s) of dsDNA binding³⁹. The Spiral has a single,

isolated interface with the Pincer domain, and it makes no other interactions to the remainder of the ATM dimer. As such, binding events that are limited to the Spiral would be unlikely to cause a movement or conformational change at the Pincer domain. With mTOR, the activator Rheb bridges one end of the N-heat solenoid to portions of mTOR that are invariant during activation, thus providing a pivot point for the movement of the other N-heat end anchored on the FAT domain⁴². While DNA-PKcs is more complex, the extensive interactions of N-heat and M-heat along their solenoids appear to similarly serve as pivot point(s) for the movement of N-heat at its FAT anchor⁴⁴. It is thus likely that dsDNA-MRN either engage additional ATM domains beyond the Spiral, or they bridge the two Spiral domains of the dimer in a manner that changes their relative orientation, with the resulting change propagating to the Pincer domains (Figure 5—figure supplement 2B).

Because the FAT domain plays a central role in the dimerization interface of the inactive ATM dimer, a conformational change in the FAT domain may well affect the relative arrangement of the two ATM protomers. This may disrupt the packing of $\kappa\alpha 9b$ with the TRD3 coiled coil from the second protomer, allowing the movement of $\kappa\alpha 9b$ to expose the P_{+1} substrate-binding site. Our steady state kinetic analysis showed that MRN+dsDNA increases the k_{cat} value of ATM phosphorylating a p53 substrate by over two orders of magnitude without affecting the K_M value (Figure 5—figure supplement 1C to H). This mirrors the steady-state kinetic constants of mTOR activation⁴². However, activation having no effect on the K_M value was unexpected, given that the presumed binding site for the P_{+1} position of the substrate is blocked in the structure. This may be analogous to findings with the canonical Cdk2-CyclinA kinase, which is activated by phosphorylation on its activation loop. Even though phosphorylation reorganizes the substrate-binding site on

the Cdk2 activation loop, the majority of the increase in catalytic efficiency is reflected in an increased rate of phosphoryl group transfer step⁶². Based on the model proposed for Cdk2⁶², it is possible that the blocked P₊₁ position in inactive ATM allows substrate binding, but with the phospho-acceptor group in an unfavorable position or orientation that reduces the rate of phosphoryl group transfer.

In conclusion, our structural data supports the model that activation of the ATM kinase domain may be mechanistically analogous to the activation of mTOR and DNA-PKcs. While it is not known how Rad50 and Mre11 interact with ATM, we find that the Nbs1 FxF/Y motif binds to the ATM Spiral domain, and the Spiral domain of Tel1 was shown to bind to dsDNA independently of MRN³⁹. Thus, it is possible that these Spiral interactions cooperate with additional contacts by MRN to trigger a motion of the Pincer domain. This would then result in a conformational change in the FAT domain that not only realigns the N and C lobes of the kinase domain but also relieves the blockage of the substrate-binding site.

Methods

Peptides, reagents, and antibodies

A peptide corresponding to the C-terminal 28aa of Nbs1 (Nc28) was purchased from Genscript and dissolved in 100mM HEPES pH 7.4 to a concentration of 2mM as measured by 205nm absorbance. No other specialty reagents or antibodies were used in this study.

Purification of ATM kinase

Codon optimized human ATM harboring an N-terminal FLAG tag was purified from a stably transfected HEK 293 cell line grown in suspension. Cells were grown to a density of 2×10^6 per liter, pelleted, and resuspended in 50 mL per liter of ATM lysis buffer containing 50 mM Tris-HCl pH 8.0, 500 mM NaCl, 50 mM KCl, 1 mM EDTA, 10 % v/v glycerol, 0.5 mM TCEP, supplemented with protease inhibitors aprotinin, leupeptin, pepstatin, AEBSF. Cells were lysed by 2 passages through a cell disruptor, and the cell lysate was clarified by centrifugation. The soluble cell lysate was incubated with α -FLAG M2 sepharose (Sigma) for 1 hour at 4° C, passed over a gravity column, and the resin was extensively washed with lysis buffer. FLAG-ATM was eluted from the resin in lysis buffer containing 0.2 mg/mL FLAG peptide. FLAG-ATM was diluted to reduce the NaCl concentration to ~100 mM and loaded onto a Mono-Q 5/50GL column equilibrated in Buffer A (25 mM Tris-Cl pH 8.0, 100 mM NaCl, and 0.5 mM TCEP). ATM was eluted from the column with a linear gradient of 0-100 % buffer B (25 mM Tris-Cl pH 8.0, 1 M NaCl, and 0.5 mM TCEP). ATM eluted at approximately 325 mM NaCl. Peak fractions were pooled and used directly for cryo-EM grid preparation. The remaining fractions containing ATM were pooled and glycerol was added to a final concentration of 10 % v/v. ATM was aliquoted, flash frozen in liquid N₂, and stored at -80° C for kinase and pull-down assays.

Purification of the MRN complex

Codon optimized human Mre11, Rad50, and Nbs1 each containing their own CMV promoters, non-cleavable C-terminal FLAG tag, and poly-A sequences were cloned into a modified pcDNA-based polycistronic mammalian expression vector. Mre11 also harbored the H129N mutation that abolishes nuclease activity. FLAG-tagged MRN was expressed

by PEI transient transfection of HEK 293 cells growing in suspension at a density of $1-2 \times 10^6$ per liter. After 48 hours cells were pelleted and resuspended in 50 mL per liter of MRN lysis buffer containing 50 mM Tris-Cl pH 8.0, 750 mM NaCl, 50 mM KCl, 10 % v/v glycerol, 0.5 mM TCEP, supplemented with protease inhibitors aprotinin, leupeptin, pepstatin, AEBSF. The remainder of the purification procedure was performed using the same protocol as ATM. Peak Mono-Q fractions were pooled, aliquoted, flash frozen in liquid N₂, and stored at -80°C for kinase assays. The MRN FRY-to-AAA mutant was generated using InFusion mutagenesis and purified in the same manner as wild-type MRN.

Cryo-EM grid preparation

For the apo ATM sample, Mono-Q purified ATM kinase was diluted to 0.6 mg/mL in 25 mM Tris-Cl pH 8.0, 300 mM NaCl, 0.5 mM TCEP, 1.25 mM AMP-PNP, and 2.5 mM MgCl₂ and incubated on ice for 1 hour. For the ATM-Nc28 sample, frozen ATM was thawed and dialyzed against 25 mM Tris-Cl pH 8.0, 250 mM NaCl, and 0.5 mM TCEP overnight. ATM was then mixed with the Nc28 peptide at final concentrations of 1.2 μM (0.42 mg/mL) and 207 μM (0.73 mg/mL), respectively. After addition of 2.5 mM AMP-PNP and 5 mM MgCl₂, the sample was incubated on ice for 1 hour. Each sample was briefly centrifuged to remove large aggregated species. The sample was applied to glow-discharged UltraAuFoil 300 mesh R1.2/1.3 grids (Quantifoil) via double-sided application of 2.5+2.5 μL. Grids were blotted for 1.5 to 3 seconds at 22° C and 95 % relative humidity and plunge frozen in liquid ethane using a FEI Vitrobot Mark IV.

Cryo-EM data collection

For the apo ATM sample, a single dataset was collected at the Memorial Sloan Kettering cryoEM Facility on a Titan Krios microscope operated at 300kEV equipped with a Gatan K3 Summit direct electron detector. Data was acquired using a defocus range of -0.6 to -1.6 μ m and a pixel size of 1.056Å. Each micrograph was acquired using a 3 second exposure and fractionated into 40 frames with a dose of 20 electrons per pixel per second. A total of 9,028 micrographs were collected using 3X3 image shift. For the ATM-Nc28 sample, a single dataset was collected at Janelia Research Campus on a Titan Krios microscope operated at 300kEV equipped with a Gatan K3 Summit direct electron detector and an energy filter. Data was acquired using a defocus range of -1.0 to -2.5 μ m and a pixel size of 1.078Å. Each micrograph was acquired using a 3 second exposure and fractionated into 40 frames with a dose of 20 electrons per pixel per second. A total of 7,866 micrographs were collected using 3X3 image shift.

Data processing and structure refinement

Beam-induced sample motions were corrected using MotionCorr2 software, and contrast transfer function parameters were estimated using CTFFIND4 software. All subsequent processing steps were performed using RELION-3 software. All reported resolutions are calculated from gold-standard refinement procedures with the FSC=0.143 criterion after post-processing by applying a soft mask, correction for the modulation transfer function (MTF) of the detector, temperature-factor sharpening, and correction of FSC curves to account for the effects of the soft mask as implemented in RELION. For apo-ATM, all processing steps are summarized in Figure 1—figure supplement 2 and 3. A total of 8,973 micrographs were selected based on a CTF estimated resolution cutoff of 10 Å. ~2.5

646 million particles were autopicked using 2D templates generated from a previously
647 collected, smaller ATM dataset collected using a Gatan K2 Summit direct electron
648 detector. Picked particles were cleaned by multiple rounds of binned and unbinned 2D and
649 3D classifications. The remaining ~1.5 million particles were subjected to 2 rounds of per-
650 particle Bayesian training, polishing and CTF refinement taking per particle astigmatism
651 and beam tilt into account. Additional rounds of 2D and 3D classifications were performed
652 after polishing to remove truncated ATM dimers. The resulting 303,604 particles were
653 refined while applying C2 symmetry to an overall resolution of 2.5 Å. An additional round of
654 3D classification using 6 classes was performed to subclassify the overall ATM dimer
655 particles into open and closed states. The most open class containing 44,152 particles and
656 the most closed class containing 44,114 particles were each refined while applying C2
657 symmetry to an overall resolution of 2.7 Å and 2.7 Å, respectively. For each particle set
658 (overall, open, and closed), partial signal subtraction and symmetry expansion procedures
659 were performed to align the ATM protomer using a soft mask generated from an initial
660 build of the ATM protomer⁴⁷. Refinements were performed using masks generated for the
661 overall promoter, N-terminal solenoids (roughly corresponding to residues 1-1588), and
662 FAT+Kinase domains including FAT-proximal portions of the N-terminal solenoids (roughly
663 corresponding to residues 1588-3056). An initial model was docked into each focused map
664 in Chimera software, and focused maps were combined using the `combine_focused_maps`
665 tool in Phenix software with the `local_weighting` flag set to True and `local_residues` set to
666 10. The final overall, open, and closed protomers were iteratively built and refined against
667 these composite maps using Coot and Phenix software. All structure and model-to-map
668 validations were performed using Molprobity tools as implemented in Phenix software

669 using composite protomer maps. The final overall, open, and closed dimers were
670 generated by applying NCS operators calculated from the corresponding C2 symmetric
671 dimer maps and refined into the corresponding dimer composite maps. For the data set of
672 the ATM-Nc28 complex, all processing steps are summarized in Figure 4—figure
673 supplement 1. A total of 6,531 micrographs were selected based on a CTF estimated
674 resolution cutoff of 5 Å. ~2 million particles were autopicked using 2D templates generated
675 from a previous ATM dataset collected using a Gatan K2 Summit direct electron detector.
676 Picked particles were cleaned by multiple rounds of binned and unbinned 2D and 3D
677 classifications, with truncated ATM dimers removed prior to polishing. The remaining
678 287,615 particles were subjected to 2 rounds of per-particle Bayesian training, polishing
679 and CTF refinement also taking per particle astigmatism and beam tilt into account. The
680 polished particles were refined while applying C2 symmetry to an overall resolution of 2.5
681 Å. Partial signal subtraction, symmetry expansion, and focused refinement procedures
682 were performed in the same manner as unbound ATM. Focused maps were combined in
683 the same manner as unbound ATM, and an initial model was refined against the
684 composite map. At this stage, we identified extra density adjacent to a hydrophobic cleft in
685 the Spiral domain of ATM. A 7-residue segment (⁷⁴²DLFRYNP⁷⁴⁸) of the Nbs1 peptide had
686 unambiguous density, especially for Phe744, Tyr746 and Pro748, and it was built into the
687 map. Because the peptide density level was lower than the surrounding ATM density, we
688 performed 3D classification without alignment to separate Nc28-bound and unbound
689 particles using RELION. For this, we used the initial Nc28 model to generate a soft mask
690 around this area including ATM residues 917 to 1101, and we performed iterative rounds
691 of focused 3D classification without alignment using particles pre-aligned on the Spiral

domain, with 3 classes and tau_fudge factor set to between 150 to 600. After multiple rounds of 3D local classification, one class containing ~75 % of the original symmetry-expanded set of particles (481,066 particles) had strong density within the pocket. Focused refinements were repeated and maps were again combined using this subset of particles. The peptide density was better defined in the resulting composite map and we were able to extend the Nbs1 model to 10-residues (⁷⁴⁰ADDLFRYNPY⁷⁴⁹). The final protomer was built and refined against this composite protomer map using Coot and Phenix software. All structure and model-to-map validations were performed using Molprobity tools as implemented in Phenix software. The final ATM-Nc28 dimer was generated by applying NCS operators calculated from the C2 symmetric dimer map and refined into the dimer composite map.

Pull-down assays

GST-tagged Nbs1 C-terminal 147 residues (GST-Nc147) harboring a C-terminal StrepII tag was expressed from a pGEX vector in *E. coli* BL21[DE3] cells. Cells were lysed by sonication and the protein was initially purified by a glutathione sepharose column. Elutions were further purified by a StrepTactin Sepharose column and eluted with 10 mM desthiobiotin (DTB). GST-Nc147 and mutants were concentrated and DTB was removed by serial buffer exchanges. Proteins were aliquoted, flash frozen in liquid N₂, and stored at -80°C. For pull-down assays, 3 µg of wild-type or mutant GST-Nc147 was coupled to 25 µL of pre-equilibrated glutathione sepharose resin in 200 µL of binding/wash (B/W) buffer containing 25 mM Tris-Cl pH 8.0, 200 mM NaCl, 0.5 mM TCEP, and 0.01 % v/v NP-40 for 1 hour with rotation at 4°C. The resin was washed once with 500 µL of B/W buffer, and

715 resuspended in 200 μ L of B/W buffer containing 0.05 mg/mL of FLAG-ATM (10 μ g per
716 reaction) and incubated for 2 hours rotating at 4°C. The resin was washed three times with
717 500 μ L of B/W buffer for 10 minutes rotating at 4°C. 25 μ L of pelleted resin was
718 resuspended in 25 μ L of 2X LDS sample buffer and boiled for 10 minutes. 25 μ L (50% of
719 the reaction) was loaded onto a 4-12% Bis-Tris SDS-PAGE gel. Proteins were separated
720 by electrophoresis and gels were stained in InstantBlue Coomassie Stain (Abcam).

721

722 ***In-vitro* kinase assays**

723 All steady-state *in-vitro* kinase assays were assembled in 10 μ L in a buffer containing 25
724 mM HEPES-Na pH 7.5, 150 mM NaCl, 1 mM MgCl_2 , 2 mM DTT, 5 % v/v glycerol, and 1
725 mg/mL native BSA. All kinase assays also contained 25 nM ATM kinase. The substrate
726 used for all kinase assays is a GST-tagged p53 fragment of 44 N-terminal residues (GST-
727 p53 residues 1-44). Reactions were assembled on ice, and started by the addition of 0.5
728 mM cold ATP supplemented with 4 μ Ci [γ - 32 P] ATP (6000 Ci/mmol, Perkin-Elmer) per
729 reaction. Reactions proceeded for 1 hour at 30°C, and were stopped by the addition of 20
730 μ L of stop buffer containing 1.5X NuPAGE LDS sample buffer, 40 mM EDTA, and 30 mM
731 TCEP. 10 μ L (1/3 of the reaction) was loaded onto a 4-12% Bis-Tris SDS-PAGE gel and
732 proteins were separated by electrophoresis. ATP standards were spotted and gels were
733 dried on DE-81 ion exchange cellulose paper. Dried gels were exposed to a phosphor
734 imaging plate and imaged on a Typhoon FLA 7000 imager. Bands were quantified using
735 ImageJ software and the concentrations of phosphorylated product and enzymatic
736 velocities were calculated based on spotted ATP standards. Velocities were normalized to

the concentration of ATM ($V/[E]$ (s^{-1})) and enzymatic parameters were calculated by fitting the data to the Michaelis-Menten equation:

$$Y = \frac{k_{cat} \times [S]}{K_M + [S]}$$

For MRN/dsDNA titrations and EC_{50} calculations (Figure 5A to C, Figure 4—figure supplement 2C, Figure 5—figure supplement 1B and D) the substrate was kept fixed at 25 μ M concentration. EC_{50} values, hill coefficients (n), and fold-activation were calculated by fitting the data to the following “[agonist] vs. response (four parameters)” equation in Prism software:

$$Y = \frac{Bottom + [activator]^n \times (Top - Bottom)}{[activator]^n + EC_{50}^n}$$

For single-turnover assays (Figure 5—figure supplement 1G), large reactions were assembled containing 250 nM ATM + 25 nM 250 bp dsDNA \pm 250 nM MRN \pm 100 nM p53 substrate and incubated at 25°C for 5 minutes. ATP containing 4 μ Ci [γ - 32 P] ATP was added at a final concentration of 0.5 mM, and reactions were incubated at 25°C. 10 μ L aliquots were removed at specified time points and mixed with 20 μ L of stop buffer. The remainder of the assay was performed in the same manner as steady-state kinase assays.

Data availability

757 The refined dimer structures and corresponding cryo-EM maps (including consensus,
758 symmetry expanded, focused, and composite maps) for unbound and Nc28-bound ATM
759 have been deposited within the Protein Data Bank (PDB) and the Electron Microscopy
760 Data Bank (EMDB) under accession codes 7SIC and EMD-25140 (unbound) and 7SID
761 and EMD-25141 (Nc28-bound).

762

763 **Acknowledgements**

764 We thank Haijuan Yang for establishing the FLAG-tagged ATM HEK 293 stable cell line
765 and establishing preliminary purification procedures. We also thank Jason De La Cruz and
766 Doreen Matthies for assistance in data collection at the MSK and HHMI cryoEM facilities,
767 respectively. This work was supported by HHMI, NIH grant CA008748 and NCI training
768 grant 5F32CA247320 (to C.W.).

769

770 **Competing interests**

771 The authors declare no competing interests.

References

1. Shiloh Y. The ATM-mediated DNA-damage response: taking shape. *Trends in Biochemical Sciences*. 2006;31(7):402-410.
doi:<https://doi.org/10.1016/j.tibs.2006.05.004>
2. Savitsky K, Bar-Shira A, Gilad S, et al. A single ataxia telangiectasia gene with a product similar to PI-3 kinase. *Science*. 1995;268(5218):1749 LP - 1753. doi:10.1126/science.7792600
3. Syed A, Tainer JA. The MRE11–RAD50–NBS1 Complex Conducts the Orchestration of Damage Signaling and Outcomes to Stress in DNA Replication and Repair. *Annual Review of Biochemistry*. 2018;87(1):263-294. doi:10.1146/annurev-biochem-062917-012415
4. Dinkelmann M, Spehalski E, Stoneham T, et al. Multiple functions of MRN in end-joining pathways during isotype class switching. *Nature Structural & Molecular Biology*. 2009;16(8):808-813.
doi:10.1038/nsmb.1639
5. Shibata A, Moiani D, Arvai AS, et al. DNA Double-Strand Break Repair Pathway Choice Is Directed by Distinct MRE11 Nuclease Activities. *Molecular Cell*. 2014;53(1):7-18.
doi:<https://doi.org/10.1016/j.molcel.2013.11.003>

- 791 6. Paull TT. Mechanisms of ATM Activation. *Annual Review of*
792 *Biochemistry*. 2015;84(1):711-738. doi:10.1146/annurev-biochem-
793 060614-034335
- 794 7. Uziel T, Lerenthal Y, Moyal L, Andegeko Y, Mittelman L, Shiloh Y.
795 Requirement of the MRN complex for ATM activation by DNA damage.
796 *The EMBO Journal*. 2003;22(20):5612 LP - 5621.
797 doi:10.1093/emboj/cdg541
- 798 8. Lee JH, Paull TT. Direct Activation of the ATM Protein Kinase by the
799 Mre11/Rad50/Nbs1 Complex. *Science*. 2004;304(5667):93 LP - 96.
800 doi:10.1126/science.1091496
- 801 9. Lee JH, Paull TT. ATM Activation by DNA Double-Strand Breaks
802 Through the Mre11-Rad50-Nbs1 Complex. *Science*.
803 2005;308(5721):551 LP - 554. doi:10.1126/science.1108297
- 804 10. Stewart GS, Maser RS, Stankovic T, et al. The DNA Double-Strand
805 Break Repair Gene hMRE11 Is Mutated in Individuals with an Ataxia-
806 Telangiectasia-like Disorder. *Cell*. 1999;99(6):577-587.
807 doi:https://doi.org/10.1016/S0092-8674(00)81547-0
- 808 11. Digweed M, Sperling K. Nijmegen breakage syndrome: clinical
809 manifestation of defective response to DNA double-strand breaks. *DNA*

- 810 *Repair*. 2004;3(8):1207-1217.
- 811 doi:<https://doi.org/10.1016/j.dnarep.2004.03.004>
- 812 12. Ragamin A, Yigit G, Bousset K, et al. Human RAD50 deficiency:
- 813 Confirmation of a distinctive phenotype. *American Journal of Medical*
- 814 *Genetics Part A*. 2020;n/a(n/a). doi:10.1002/ajmg.a.61570
- 815 13. Lukas C, Melander F, Stucki M, et al. Mdc1 couples DNA double-strand
- 816 break recognition by Nbs1 with its H2AX-dependent chromatin retention.
- 817 *The EMBO Journal*. 2004;23(13):2674-2683.
- 818 doi:10.1038/sj.emboj.7600269
- 819 14. Haince JF, McDonald D, Rodrigue A, et al. PARP1-dependent Kinetics
- 820 of Recruitment of MRE11 and NBS1 Proteins to Multiple DNA Damage
- 821 Sites. *Journal of Biological Chemistry* . 2008;283(2):1197-1208.
- 822 doi:10.1074/jbc.M706734200
- 823 15. Hoa NN, Shimizu T, Zhou ZW, et al. Mre11 Is Essential for the Removal
- 824 of Lethal Topoisomerase 2 Covalent Cleavage Complexes. *Molecular*
- 825 *Cell*. 2016;64(3):580-592.
- 826 doi:<https://doi.org/10.1016/j.molcel.2016.10.011>
- 827 16. Myler LR, Gallardo IF, Soniat MM, et al. Single-Molecule Imaging
- 828 Reveals How Mre11-Rad50-Nbs1 Initiates DNA Break Repair. *Molecular*

- 829 *cell*. 2017;67(5):891-898.e4. doi:10.1016/j.molcel.2017.08.002
- 830 17. Symington LS, Gautier J. Double-strand break end resection and repair
831 pathway choice. *Annual review of genetics*. 2011;45:247-271.
832 doi:10.1146/annurev-genet-110410-132435
- 833 18. de Jager M, van Noort J, van Gent DC, Dekker C, Kanaar R, Wyman C.
834 Human Rad50/Mre11 Is a Flexible Complex that Can Tether DNA Ends.
835 *Molecular Cell*. 2001;8(5):1129-1135. doi:https://doi.org/10.1016/S1097-
836 2765(01)00381-1
- 837 19. Hopfner KP, Craig L, Moncalian G, et al. The Rad50 zinc-hook is a
838 structure joining Mre11 complexes in DNA recombination and repair.
839 *Nature*. 2002;418:562.
- 840 20. Moreno-Herrero F, de Jager M, Dekker NH, Kanaar R, Wyman C,
841 Dekker C. Mesoscale conformational changes in the DNA-repair
842 complex Rad50/Mre11/Nbs1 upon binding DNA. *Nature*.
843 2005;437(7057):440-443. doi:10.1038/nature03927
- 844 21. Kobayashi J, Tauchi H, Sakamoto S, et al. NBS1 localizes to γ -H2AX
845 foci through interaction with the FHA/BRCT domain. *Current Biology*.
846 2002;12(21):1846-1851. doi:10.1016/S0960-9822(02)01259-9
- 847 22. Spycher C, Miller ES, Townsend K, et al. Constitutive phosphorylation of

- 848 MDC1 physically links the MRE11-RAD50-NBS1 complex to damaged
849 chromatin. *The Journal of cell biology*. 2008;181(2):227-240.
850 doi:10.1083/jcb.200709008
- 851 23. Williams RS, Dodson GE, Limbo O, et al. Nbs1 Flexibly Tethers Ctp1
852 and Mre11-Rad50 to Coordinate DNA Double-Strand Break Processing
853 and Repair. *Cell*. 2009;139(1):87-99. doi:10.1016/j.cell.2009.07.033
- 854 24. Schiller CB, Lammens K, Guerini I, et al. Structure of Mre11-Nbs1
855 complex yields insights into ataxia-telangiectasia-like disease mutations
856 and DNA damage signaling. *Nature structural & molecular biology*.
857 2012;19(7):693-700. doi:10.1038/nsmb.2323
- 858 25. You Z, Chahwan C, Bailis J, Hunter T, Russell P. ATM Activation and Its
859 Recruitment to Damaged DNA Require Binding to the C Terminus of
860 Nbs1. *Molecular and Cellular Biology*. 2005;25(13):5363 LP - 5379.
861 doi:10.1128/MCB.25.13.5363-5379.2005
- 862 26. Hailemariam S, Kumar S, Burgers PM. Activation of Tel1ATM kinase
863 requires Rad50 ATPase and long nucleosome-free DNA but no DNA
864 ends. *Journal of Biological Chemistry* . 2019;294(26):10120-10130.
865 doi:10.1074/jbc.RA119.008410
- 866 27. Oh J, Al-Zain A, Cannavo E, Cejka P, Symington LS. Xrs2 Dependent

- 867 and Independent Functions of the Mre11-Rad50 Complex. *Molecular*
868 *cell*. 2016;64(2):405-415. doi:10.1016/j.molcel.2016.09.011
- 869 28. Oh J, Lee SJ, Rothstein R, Symington LS. Xrs2 and Tel1 Independently
870 Contribute to MR-Mediated DNA Tethering and Replisome Stability. *Cell*
871 *Reports*. 2018;25(7):1681-1692.e4.
872 doi:<https://doi.org/10.1016/j.celrep.2018.10.030>
- 873 29. Falck J, Coates J, Jackson SP. Conserved modes of recruitment of
874 ATM, ATR and DNA-PKcs to sites of DNA damage. *Nature*.
875 2005;434(7033):605-611. doi:10.1038/nature03442
- 876 30. Stracker TH, Morales M, Couto SS, Hussein H, Petrini JHJ. The carboxy
877 terminus of NBS1 is required for induction of apoptosis by the MRE11
878 complex. *Nature*. 2007;447:218.
- 879 31. Imseng S, Aylett CHS, Maier T. Architecture and activation of
880 phosphatidylinositol 3-kinase related kinases. *Current Opinion in*
881 *Structural Biology*. 2018;49:177-189.
882 doi:<https://doi.org/10.1016/j.sbi.2018.03.010>
- 883 32. Lovejoy CA, Cortez D. Common mechanisms of PIKK regulation. *DNA*
884 *Repair*. 2009;8(9):1004-1008.
885 doi:<https://doi.org/10.1016/j.dnarep.2009.04.006>

- 886 33. Baretić D, Williams RL. PIKKs — the solenoid nest where partners and
887 kinases meet. *Current Opinion in Structural Biology*. 2014;29:134-142.
888 doi:<https://doi.org/10.1016/j.sbi.2014.11.003>
- 889 34. Baretić D, Pollard HK, Fisher DI, et al. Structures of closed and open
890 conformations of dimeric human ATM. *Science Advances*.
891 2017;3(5):e1700933. doi:10.1126/sciadv.1700933
- 892 35. Langer LM, Gat Y, Bonneau F, Conti E. Structure of substrate-bound
893 SMG1-8-9 kinase complex reveals molecular basis for phosphorylation
894 specificity. Cole PA, Grigorieff N, Yaffe MB, eds. *eLife*. 2020;9:e57127.
895 doi:10.7554/eLife.57127
- 896 36. Brown NR, Noble MEM, Endicott JA, Johnson LN. The structural basis
897 for specificity of substrate and recruitment peptides for cyclin-dependent
898 kinases. *Nature Cell Biology*. 1999;1(7):438-443. doi:10.1038/15674
- 899 37. Xiao J, Liu M, Qi Y, et al. Structural insights into the activation of ATM
900 kinase. *Cell Research*. 2019;29(8):683-685. doi:10.1038/s41422-019-
901 0205-0
- 902 38. Xin J, Xu Z, Wang X, Tian Y, Zhang Z, Cai G. Structural basis of
903 allosteric regulation of Tel1/ATM kinase. *Cell Research*. 2019;29(8):655-
904 665. doi:10.1038/s41422-019-0176-1

- 905 39. Jansma M, Linke-Winnebeck C, Eustermann S, et al. Near-Complete
906 Structure and Model of Tel1ATM from *Chaetomium thermophilum*
907 Reveals a Robust Autoinhibited ATP State. *Structure*. 2020;28(1):83-
908 95.e5. doi:<https://doi.org/10.1016/j.str.2019.10.013>
- 909 40. Yates LA, Williams RM, Hailemariam S, Ayala R, Burgers P, Zhang X.
910 Cryo-EM Structure of Nucleotide-Bound Tel1ATM Unravels the
911 Molecular Basis of Inhibition and Structural Rationale for Disease-
912 Associated Mutations. *Structure*. 2020;28(1):96-104.e3.
913 doi:<https://doi.org/10.1016/j.str.2019.10.012>
- 914 41. Yang H, Rudge DG, Koos JD, Vaidialingam B, Yang HJ, Pavletich NP.
915 mTOR kinase structure, mechanism and regulation. *Nature*.
916 2013;497(7448):217-223. doi:10.1038/nature12122
- 917 42. Yang H, Jiang X, Li B, et al. Mechanisms of mTORC1 activation by
918 RHEB and inhibition by PRAS40. *Nature*. 2017;552(7685):368-373.
919 doi:10.1038/nature25023
- 920 43. Sibanda BL, Chirgadze DY, Ascher DB, Blundell TL. DNA-PKcs
921 structure suggests an allosteric mechanism modulating DNA double-
922 strand break repair. *Science*. 2017;355(6324):520 LP - 524.
923 doi:10.1126/science.aak9654

- 924 44. Chen X, Xu X, Chen Y, et al. Structure of an activated DNA-PK and its
925 implications for NHEJ. *Molecular Cell*. Published online 2020.
926 doi:<https://doi.org/10.1016/j.molcel.2020.12.015>
- 927 45. Chen S, Lee L, Naila T, et al. Structural basis of long-range to short-
928 range synaptic transition in NHEJ. *Nature*. 2021;593(7858):294-298.
929 doi:10.1038/s41586-021-03458-7
- 930 46. Chaplin AK, Hardwick SW, Stavridi AK, et al. Cryo-EM of NHEJ
931 supercomplexes provides insights into DNA repair. *Molecular Cell*.
932 2021;81(16):3400-3409.e3. doi:10.1016/j.molcel.2021.07.005
- 933 47. Scheres SHW. Chapter Six - Processing of Structurally Heterogeneous
934 Cryo-EM Data in RELION. In: Crowther RABTM in E, ed. *The Resolution*
935 *Revolution: Recent Advances In CryoEM*. Vol 579. Academic Press;
936 2016:125-157. doi:<https://doi.org/10.1016/bs.mie.2016.04.012>
- 937 48. Stakyte K, Rotheneder M, Lammens K, et al. Molecular basis of human
938 ATM kinase inhibition. *Nature Structural & Molecular Biology*. Published
939 online 2021. doi:10.1038/s41594-021-00654-x
- 940 49. Wang X, Chu H, Lv M, et al. Structure of the intact ATM/Tel1 kinase.
941 *Nature Communications*. 2016;7(1):11655. doi:10.1038/ncomms11655
- 942 50. Krissinel E, Henrick K. Inference of Macromolecular Assemblies from

- 943 Crystalline State. *Journal of Molecular Biology*. 2007;372(3):774-797.
944 doi:<https://doi.org/10.1016/j.jmb.2007.05.022>
- 945 51. Bakkenist CJ, Kastan MB. DNA damage activates ATM through
946 intermolecular autophosphorylation and dimer dissociation. *Nature*.
947 2003;421:499.
- 948 52. Pellegrini M, Celeste A, Difilippantonio S, et al. Autophosphorylation at
949 serine 1987 is dispensable for murine Atm activation in vivo. *Nature*.
950 2006;443(7108):222-225. doi:10.1038/nature05112
- 951 53. Knighton DR, Zheng JH, Ten Eyck LF, Xuong NH, Taylor SS, Sowadski
952 JM. Structure of a Peptide Inhibitor Bound to the Catalytic Subunit of
953 Cyclic Adenosine Monophosphate-Dependent Protein Kinase. *Science*.
954 1991;253(5018):414-420. doi:10.1126/science.1862343.
- 955 54. Bao ZQ, Jacobsen DM, Young MA. Briefly Bound to Activate: Transient
956 Binding of a Second Catalytic Magnesium Activates the Structure and
957 Dynamics of CDK2 Kinase for Catalysis. *Structure*. 2011;19(5):675-690.
958 doi:<https://doi.org/10.1016/j.str.2011.02.016>
- 959 55. Jacobsen DM, Bao ZQ, O'Brien P, Brooks CL, Young MA. Price To Be
960 Paid for Two-Metal Catalysis: Magnesium Ions That Accelerate
961 Chemistry Unavoidably Limit Product Release from a Protein Kinase.

962 *Journal of the American Chemical Society*. 2012;134(37):15357-15370.
 963 doi:10.1021/ja304419t

964 56. Vadas O, Burke JE, Zhang X, Berndt A, Williams RL. Structural Basis for
 965 Activation and Inhibition of Class I Phosphoinositide 3-Kinases. *Science*
 966 *Signaling*. 2011;4(195):re2 LP-re2. doi:10.1126/scisignal.2002165

967 57. Ogi H, Goto GH, Ghosh A, Zencir S, Henry E, Sugimoto K. Requirement
 968 of the FATC domain of protein kinase Tel1 for localization to DNA ends
 969 and target protein recognition. *Molecular biology of the cell*.
 970 2015;26(19):3480-3488. doi:10.1091/mbc.E15-05-0259

971 58. Buis J, Wu Y, Deng Y, et al. Mre11 Nuclease Activity Has Essential
 972 Roles in DNA Repair and Genomic Stability Distinct from ATM
 973 Activation. *Cell*. 2008;135(1):85-96.
 974 doi:https://doi.org/10.1016/j.cell.2008.08.015.

975 59. Lee J, Paull TTB in E. Purification and Biochemical Characterization
 976 of Ataxia - Telangiectasia Mutated and Mre11/Rad50/Nbs1. In: *DNA*
 977 *Repair, Part A*. Vol 408. Academic Press; 2006:529-539.
 978 doi:https://doi.org/10.1016/S0076-6879(06)08033-5

979 60. Mordes DA, Glick GG, Zhao R, Cortez D. TopBP1 activates ATR
 980 through ATRIP and a PIKK regulatory domain. *Genes & Development*.

2008;22(11):1478-1489. doi:10.1101/gad.1666208

61. Rao Q, Liu M, Tian Y, et al. Cryo-EM structure of human ATR-ATRIP complex. *Cell Research*. 2018;28(2):143-156. doi:10.1038/cr.2017.158
62. Hagopian JC, Kirtley MP, Stevenson LM, et al. Kinetic Basis for Activation of CDK2/Cyclin A by Phosphorylation*. *Journal of Biological Chemistry*. 2001;276(1):275-280. doi:<https://doi.org/10.1074/jbc.M007337200>

Figure legends

Figure 1: Overall structure of the human ATM kinase.

A) Domain map of the human ATM kinase showing Spiral (residues 1-1166), Pincer (1167-1898), FAT (1899-2613), Kinase (2614-3026), and FATC (3027-3056) domains. FAT domain is further divided into TRD1 (1899-2025), TRD2 (2026-2192), TRD3 (2193-2479), and HRD (2480-2613) subdomains. Kinase domain is further divided into N-lobe (2614-2770), C-lobe (2771-2957), and PRD (2958-3026) subdomains. **B)** Composite cryo-EM density map of ATM kinase colored by approximate domain location. AMP-PNP molecule and Mg^{2+} ion in the active site colored cyan and gray, respectively. **C)** Structure of the overall ATM dimer colored by domain.

Figure 2: Details of the FAT domain and dimer interface of ATM.

A) Domain map of the FATKD colored by subdomain as in Figure 1A. **B)** Structure of the FATKD colored by domain as in Figure 1A showing side, top and bottom views. AMP-PNP molecule and single magnesium ion colored cyan and gray, respectively. **C)** Structure of the FATKD with one chain colored gray to highlight intermolecular contacts. **D)** Intermolecular helical packing within the upper dimer interface by FAT helices $\alpha 4-8$ located within the TRD2 subdomain. **E)** Details of the contacts between the long coiled coil of TRD3 ($\alpha 21-22$) with the $\alpha 9b$ of the PRD of the symmetric ATM protomer. **F)** Contacts between $\alpha 19-20$ of TRD3 with the FATC of the symmetric ATM protomer.

Figure 3: Details of the kinase domain and active site of ATM.

A) Structure of the Kinase, PRD, and FATC domains with secondary structure elements labeled. Also highlighted are the locations of the catalytic loop (residues 2866-2875, blue) and activation loop (residues 2888-2911, green). AMP-PNP and a single magnesium ion in the active site colored cyan and gray, respectively. **B)** Details of the interactions within the active site. Critical residues within the N lobe, C lobe, catalytic and activation loops are shown as sticks and labeled. **C)** Electron density around AMP-PNP and Mg^{2+} cofactors contoured to 5σ . **D)** Steric occlusion of the γ phosphate of AMP-PNP by residues V2696 and N2697 on the N lobe and Y2969 on $\alpha 9b$ of the PRD. **E)** Salt-bridge formed between K3016 (PRD, $\alpha 10$) to E2895 (activation loop). K3016 is acetylated during the DNA-damage response and correlates with active ATM kinase. **F)** Alignment of the Kinase domain of ATM with those of mTOR and DNA-PKcs in the inactive and active states. Structures are aligned along their corresponding catalytic and activation loops. ATM N and C lobes are colored yellow and pink, respectively. Inactive and active mTOR are colored

orange and cyan, respectively. Inactive and active DNA-PKcs are colored red and green, respectively. Arrow indicates movement of the N lobe relative to the C lobe coincident with mTOR and DNA-PKcs activation. **G)** Positions of catalytically important residues relative to those of mTOR in the inactive and active states. **H)** Positions of catalytically important residues relative to those of DNA-PKcs in the inactive and active states.

Figure 4: Structure of ATM bound to the C-terminus of Nbs1.

A) Alignment of the Nbs1 C-terminal 28 residues (Nc28) from 24 vertebrate species showing the conservation of the C-terminus and FxF/Y motif. Portion of Nc28 visible in the cryo-EM map is highlighted in magenta. **B)** Location of the Nc28 bound to the ATM Spiral domain in the composite map (left) and structure (right). Nc28 is colored magenta. **C)** Zoom of the location of the Nc28 peptide showing Phe744 inserted into a hydrophobic groove made up of ATM helices α 39 to α 42. Nc28 peptide density is contoured to 4σ . **D)** Details of the interaction between Nc28 and the ATM Spiral, showing Phe744 inserted into a hydrophobic pocket created by ATM residues Arg981, Cys987, Val1021, Ala1024, Phe1025, Leu1028, and Tyr1034. Arg745 of Nbs1 makes electrostatic contacts with ATM Asn975 and Ser978. Tyr746 of Nbs1 packs against the α 41. Nbs1 L743 makes contacts with an adjacent hydrophobic cleft created by ATM residues Leu1028 and His1064. Nbs1 Asp741 makes electrostatic and H-bonding contacts with ATM residues Arg981 and Ser978, respectively. **E)** ATM pull-down assay using GST-tagged Nbs1 C-terminal 147 residues (GST-Nc147) as bait. Lanes are labeled at the top of the image, and bands are labeled on the right. Asterisk indicates Hsp70/DnaK contaminant that co-purifies with all GST-Nc147 preparations.

Figure 5: ATM activation requires MRN and long dsDNA, but not the FxF/Y motif of Nbs1

A) Top: Steady-state ATM kinase assay using 25 nM ATM, 250 nM MRN and 25 μ M p53 substrate with 2.5 ng/ μ L of dsDNA of various lengths added. **Bottom:** Quantification of ATM enzymatic velocity as a function of DNA length. 3 biological replicates per point. Curve fit to the EC₅₀ equation. **B) Top:** Steady-state ATM kinase assay using 25 nM ATM, 250 nM MRN and 25 μ M p53 substrate with various concentrations (0.5 to 5 ng/ μ L) of 100bp, 250bp and 500bp dsDNA fragments. 150 ng/ μ L 100bp dsDNA is in the upper right lane. **Bottom:** Quantification of ATM enzymatic velocity as a function of DNA concentration. 3 biological replicates per point, Curve fit to the EC₅₀ equation. **C) Top:** Steady-state ATM kinase assay using 25 nM ATM, 25 nM 350bp dsDNA, and various concentrations of wild-type or FRY to AAA mutant MRN. **Bottom:** Quantification of ATM enzymatic velocity as a function of MRN concentration. 3-6 biological replicates per point. Curves fit to the EC₅₀ equation.

Supplemental figure legends

Figure 1—figure supplement 1: Purification and basal activity of ATM kinase.

A) SDS-PAGE of purified FLAG-tagged ATM kinase. 1, 2 and 5 μ g of protein were run on the gel. **B) Top:** Steady-state kinase assay of ATM with various concentrations of GST-tagged p53 N-terminal 44 residue substrate (GST-p53 1 to 44) with no dsDNA or MRN added. **Bottom:** Quantification of enzymatic parameters (K_M , n_H , and k_{cat}) of ATM toward

GST-tagged p53 peptide substrate. 3 biological replicates per point. Curve fit to the Michaelis-Menten equation.

Figure 1—figure supplement 2: Cryo-EM data processing of the apo ATM sample.

A) Example micrograph of ATM. **B)** Example 2D class averages of ATM. **C)** Workflow of ATM cryo-EM data analysis. Rainbow maps are colored by local resolution, color scale at bottom left. **D)** Fourier shell correlation (FSC) curves of B-factor sharpened overall, open, and closed ATM dimer maps. Gold-standard resolution threshold (FSC=0.143) shown as a dashed line. **E)** Angular distribution of ATM particles in the overall consensus refinement with C2 symmetry imposed.

Figure 1—figure supplement 3: Partial signal subtraction, symmetry expansion and focused refinement procedure for ATM.

A) Graphic of the partial signal subtraction, symmetry expansion and focused refinement procedure. FATKD and HEAT-focused refinement maps shown in orange and magenta boxes on right, respectively. All maps colored by local resolution based on the scale on the right. **B)** Electron density snapshots of helices within the Spiral, Pincer, FAT, and Kinase/FATC domains. Helices colored according to domain as in Figure 1A. Corresponding residue numbers are displayed at the top and bottom of each helix. All maps are contoured to 7σ . **C)** FSC curves of B-factor sharpened overall, open, and closed protomer maps, including FATKD and HEAT focused maps for each. Gold-standard resolution threshold (FSC=0.143) shown as a dashed line.

Figure 1—figure supplement 4: Secondary structure and sequence conservation of human ATM.

A) Sequence of human ATM kinase showing CONSURF scores as bar graph for each residue. STRIDE-calculated secondary structures of the overall protomer are mapped onto the sequence. Helices are shown as rectangles, sheets as arrows, and coils as solid lines. Disordered regions not built in our structure are shown as dashed lines. Secondary structures are colored by domain as in Figure 1A and labeled.

Figure 1—figure supplement 5: Positions and frequencies of cancer-associated ATM missense mutations.

A) Positions and frequencies of cancer associated missense mutations from the COSMIC database along the sequence of ATM. The three most prevalent missense mutations are labeled. **B)** Positions of cancer associated missense mutations from the COSMIC database mapped onto the overall ATM dimer structure as spheres. Frequencies of each mutation shown by color scale (right of figure). Positions with less than 3 COSMIC-annotated mutations are not displayed for clarity. **C)** Positions and frequencies of cancer associated missense mutations within the ATM kinase domain. AMP-PNP and magnesium ion colored cyan and gray, respectively. **D)** Positions and frequencies of ATM cancer associated missense mutations within the Nbs1 binding cleft. Nbs1 C-terminal peptide (Nc28) shown as magenta sticks. Frequent mutations that may impact Nbs1 binding are labeled. **E)** Table of ATM missense mutations, frequencies, and associated cancer types

that may interfere with Nbs1 binding. **F)** Table of all Nbs1 missense mutations, frequencies, and associated cancer types from the C-terminal 28 amino acids.

Figure 1—figure supplement 6: Flexibility of the ATM spiral and pincer domains.

A) Structure of the most open class of the ATM dimer. C α -C α distance between protomers from residue Ile10 on α 1 shown. **B)** Structure of the most closed class of the ATM dimer. C α -C α distance between protomers from residue Ile10 on α 1 shown. **C)** Alignment of the Spiral and Pincer domains of the most open and closed ATM protomers. Open structure is colored light blue, closed structure is colored red. **D)** Structure of the Spiral and Pincer domains of the most open ATM protomer colored by C α positional RMSD (0-10Å, blue to red) compared to the closed protomer. Generated by the ColorByRMSD PyMOL script. **E)** Alignment of the FATKD of the most open and most closed classes. Overall C α positional RMSD = 0.39 Å. **F)** Alignment of the kinase domains of the most open and closed classes. Overall C α positional RMSD = 0.24 Å.

Figure 1—figure supplement 7: Surface properties of the ATM protomer.

A) Overall ATM protomer colored by APBS-calculated surface potential. Charge scale shown on the right. **B)** Overall ATM protomer colored by CONSURF sequence conservation scores. Conservation scale shown on the right. **C)** Overall ATM protomer colored by relative hydrophobicity. Relative hydrophobicity scale shown on the right. **D)** Left: zoom on the dimer interface including FAT, Kinase, and FATC domains showing multiple large hydrophobic patches. Right: Identical view showing FAT, Kinase, and FATC

domain helices from the symmetric protomer as gray tubes that shield hydrophobic patches in the dimer structure.

Figure 3—figure supplement 1: Blockage of the substrate-binding site.

A) Structure of ATM catalytic cleft showing Gln2971 hydrogen bonding to backbone amide and carbonyl groups of Thr2902 on the activation loop, anchored between hydrophobic residues Leu2900 and Phe3049. **B)** Structure of Smg1 catalytic cleft bound to a Upf1 substrate peptide (PDB: 6Z3R) showing Gln1079 in the P₊₁ position hydrogen bonding to backbone amide and carbonyl groups of Val2367 on the activation loop, anchored between hydrophobic residues Leu2365 and Tyr3654. **C)** Alignment of the activation loops of ATM and Smg1 showing the blockage of the substrate binding site by ATM Gln2971.

Figure 4—figure supplement 1: Cryo-EM data processing of the ATM-Nc28 sample.

A) Example micrograph of ATM-Nc28. **B)** Example 2D class averages of ATM-Nc28. **C)** Workflow of ATM-Nc28 cryo-EM data analysis. Rainbow consensus map is colored by local resolution, color scale on the right. **D)** Electron density within the hydrophobic pocket of ATM without and with the Nc28 peptide in the sample. Rows show two different views of the hydrophobic pocket. First column of images shows minimal electron density in this region in the HEAT-focused overall apo map (607,208 particles). Second column shows much stronger density in this region in the HEAT-focused ATM-Nc28 map (481,066 particles). Third column shows the model of the Nc28 peptide structure built into the density shown in the second column. All maps are contoured to 6 σ . **E)** Fourier shell

correlation (FSC) curves of the ATM-Nc28 dimer and protomer maps, including FATKD and HEAT-focused maps. Gold-standard resolution threshold (FSC=0.143) shown as a dashed line. **F)** Angular distribution of ATM-Nc28 particles in the overall consensus refinement with C2 symmetry imposed. **G)** Focused refinement of the symmetry expanded Spiral+Pincer domains of ATM-Nc28 particles using the same procedure as detailed in Figure S3A. Map is colored by local resolution based on the scale to the left. Boxed area shows the local resolution of the Nc28 peptide, with the map contoured to a high level for clarity.

Figure 4—figure supplement 2: Structural assessment of ATM bound to the Nc28 peptide.

A) Alignment and sequence conservation of ATM Spiral domain residues 956-1046 from 24 vertebrate species. Residue numbers and secondary structures are displayed according to the human ATM. **B)** Nbs1 peptide binding site shown as surface representation colored by APBS-calculated surface potential (left), hydrophobicity (middle), or CONSURF score (right). Same coloring scheme used as in Figure S7. **C)** Steady-state ATM kinase assay using 25nM ATM, 2.5ng/μL 350bp dsDNA, 25μM p53 substrate, and various concentrations of the Nc28 peptide showing no increase in catalytic activity. Reactions were performed 3 times with similar results. **D)** Structural alignment of the kinase domains of apo (green) and Nc28-bound (magenta) ATM. Overall Cα positional RMSD = 0.29 Å. **E)** Comparison of the structures of Nc28 bound to the ATM Spiral domain (top) and the C-terminus of Ku80 bound to the DNA-PKcs M-HEAT domain (bottom) (PDB: 7K0Y).

Figure 5—figure supplement 1: Quantitative ATM kinase assays.

A) SDS-PAGE of purified FLAG-tagged MRN. 1, 2 and 5 μg of protein were run on the gel.

B) Top: Steady-state kinase assay using 25 nM ATM, 25 μM p53 substrate, and various concentrations of MRN. **Bottom:** Quantification of ATM enzymatic velocity as a function of MRN concentration. 3 biological replicates per point. Curve fit to the EC_{50} equation. **C)**

Steady-state kinase assay using 25nM 250 bp dsDNA + 250nM MRN + 25 μM p53 substrate \pm 25nM ATM showing ATM-dependent kinase activity toward the p53 substrate. Reactions were performed 3 times with similar results. **D)** Quantification of ATM enzymatic

velocity as a function of DNA concentration. Same data used as in Figure 5B with the x-axis rescaled to molar DNA concentration. 3 biological replicates per point. Curve fit to the EC_{50} equation. **E) Top:** Steady-state kinase assay using 25 nM ATM, 25 nM 350bp

dsDNA, and various concentrations of p53 substrate peptide without and with 250 nM MRN added. **Bottom:** Quantification of ATM enzymatic velocity as a function of substrate concentration without (black) and with (blue) MRN present. 3 biological replicates per point. Curve fit to the Michaelis-Menten equation. **F)** Quantification of enzymatic

parameters (K_M and k_{cat}) of ATM under various conditions from data in Figures S1B and S11E. **G)** Time-course kinase assay run under single-turnover conditions using 250 nM ATM + 25 nM 250bp dsDNA \pm 250 nM MRN \pm 100 nM p53 substrate peptide.

Phosphorylation products are labeled on the right. Reactions were performed 3 times with similar results. **H)** Data from Figures S1B, S11B, and S11E rescaled to show fold activation relative to ATM alone at 25 μM substrate concentration. 3 biological replicates per group.

Figure 5—figure supplement 2: Structural conservation of the FAT domain anchor and model of FATKD activation.

A) Alignment of the TRD2-TRD3 interface helices from ATM, mTOR, and DNA-PKcs inactive structures (gray). ATM FAT domain helices $\alpha 10$ to $\alpha 15$ are labeled on the left. ATM Pincer helices $\alpha 21$ to $\alpha 24$ labeled on the right. Four helix bundles from the mTOR and DNA-PKcs N-HEAT domains are shown in blue and green, respectively. **B) Top:** Structure of the ATM protomer FATKD + Pincer 4-helix bundle (residues 1606-1691) in the inactive state. **Middle:** Cartoon model of the inactive structure shown above with approximate locations of FAT subdomains labeled. **Bottom:** Cartoon model of the likely structural changes that coincide with ATM activation. MRN-dsDNA binding is not shown, but most likely occurs in the Spiral domain. In this model, MRN-dsDNA binding to the Spiral domain causes a conformational change that is transmitted through the HEAT-repeats to ultimately pull on the Pincer 4-helix bundle (1). This motion, in turn, stretches and twists the TRD2, TRD3, and HRD subdomains of the FAT (2), whereas the TRD1 subdomain remains anchored on the C lobe. The motion alters the HRD-N lobe interface allowing the N lobe to undergo a slight conformational closure to realign critical catalytic residues (3), as detailed in Figure 3F. This motion of the Kinase domain, alongside motions of the FAT domain of the symmetric protomer (not shown), also allow $\kappa 9b$ to vacate the substrate binding site (4). Both the realigning of catalytic residues within the cleft (3) and the removal of the substrate block (4) are likely required for complete ATM activation.

1226 **Supplementary File 1: Cryo-EM data processing and refinement table.**

1227

1228 **Video 1: Conformational flexibility of the ATM Spiral and Pincer domains.**

1229

1230 **Source Data Titles**

1231 **Figure 4E: Nbs1 pull down assay.**

1232 **Figure 5A: ATM kinase assay with MRN and varying DNA length.**

1233 **Figure 5B: ATM kinase assay with MRN and varying DNA concentration.**

1234 **Figure 5C: ATM kinase assay with DNA and using wild-type MRN or FRY to AAA**

1235 **mutant.**

1236 **Figure 1 – figure supplement 1A: SDS-PAGE of purified ATM kinase.**

1237 **Figure 1 – figure supplement 1B: ATM kinase assay without MRN or DNA.**

1238 **Figure 4 – figure supplement 2C: ATM kinase assay with DNA and Nc28.**

1239 **Figure 5 – figure supplement 1A: SDS-PAGE of purified MRN complex.**

1240 **Figure 5 – figure supplement 1B: ATM kinase assay with MRN and without DNA.**

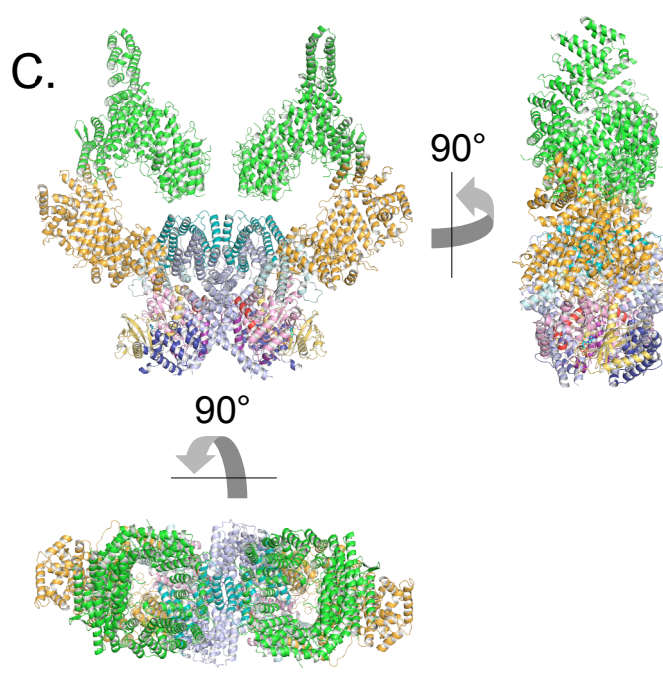
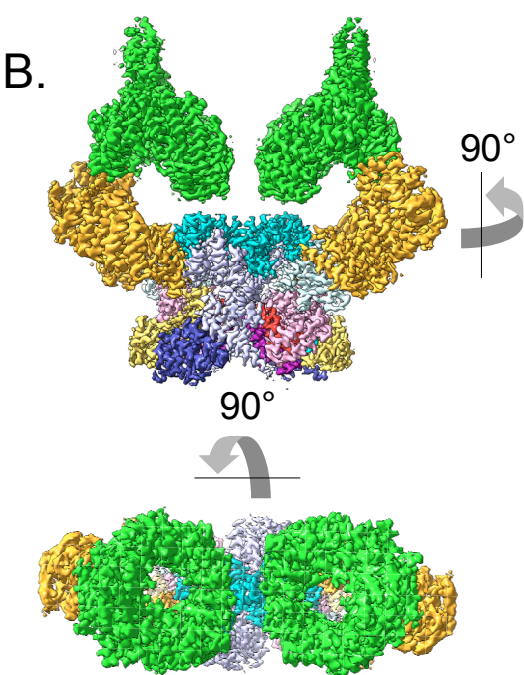
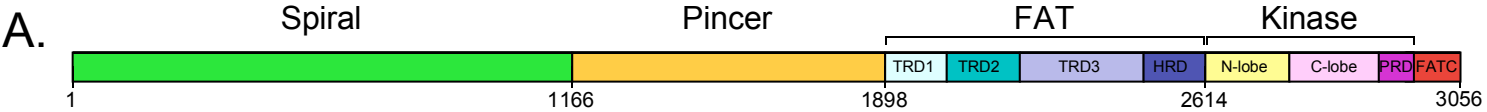
1241 **Figure 5 – figure supplement 1C: ATM kinase assay with DNA and MRN, without and**

1242 **with ATM.**

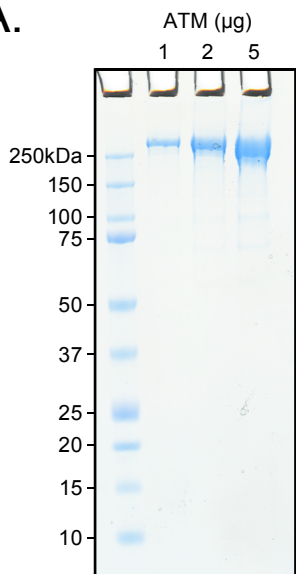
1243 **Figure 5 – figure supplement 1E: ATM kinase assay with DNA, without and with**

1244 **MRN.**

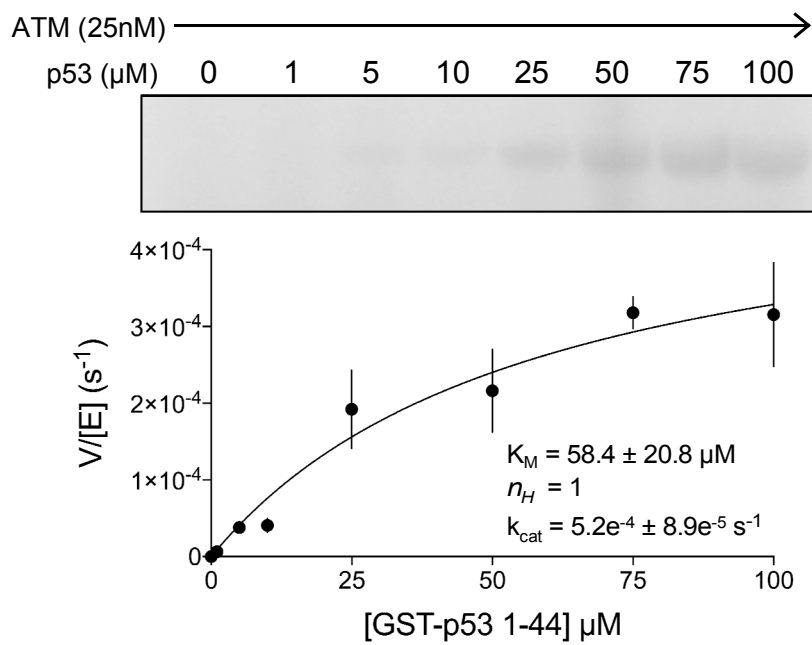
1245 **Figure 5 – figure supplement 1G: Single-turnover ATM kinase assay.**

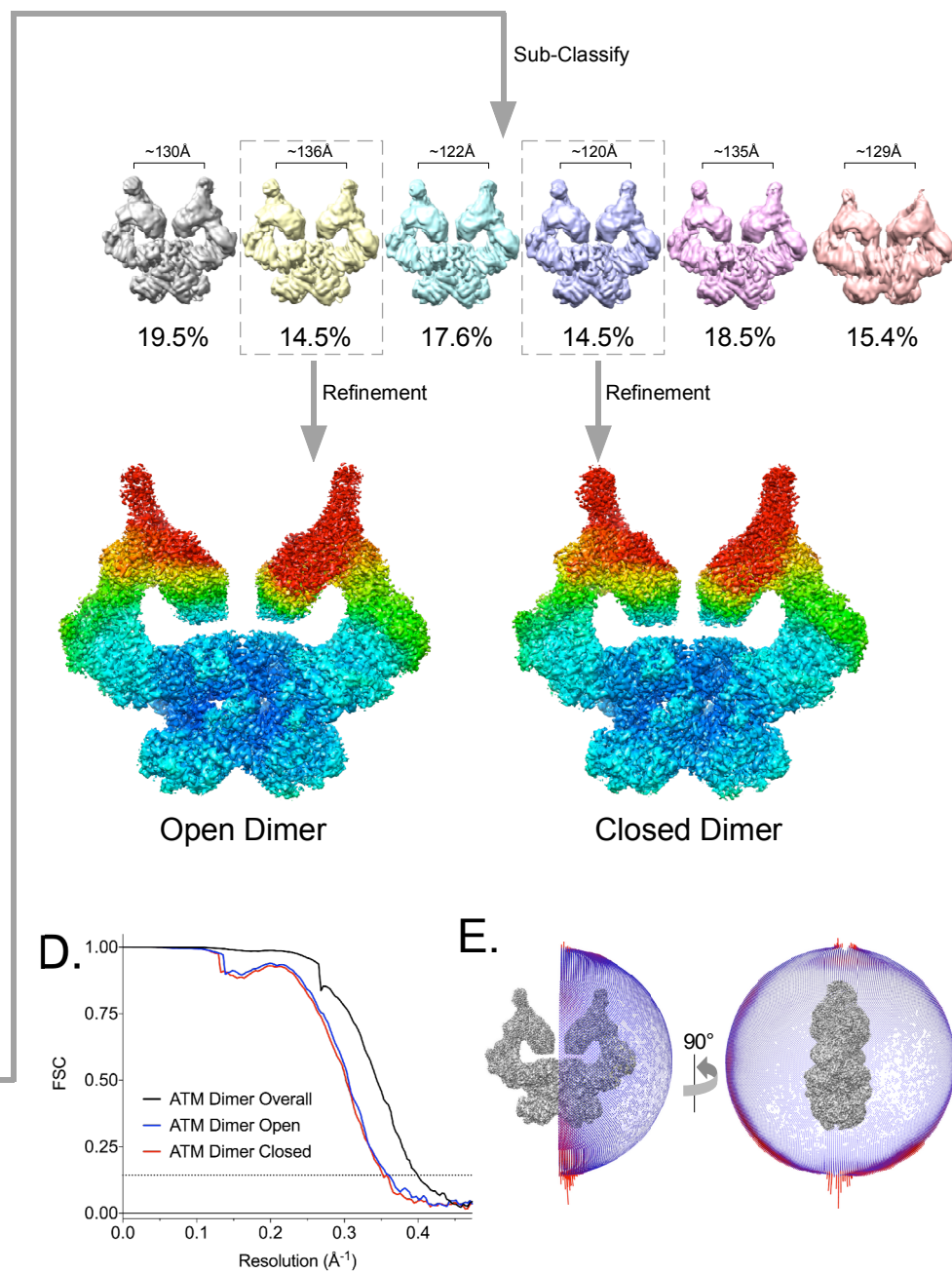
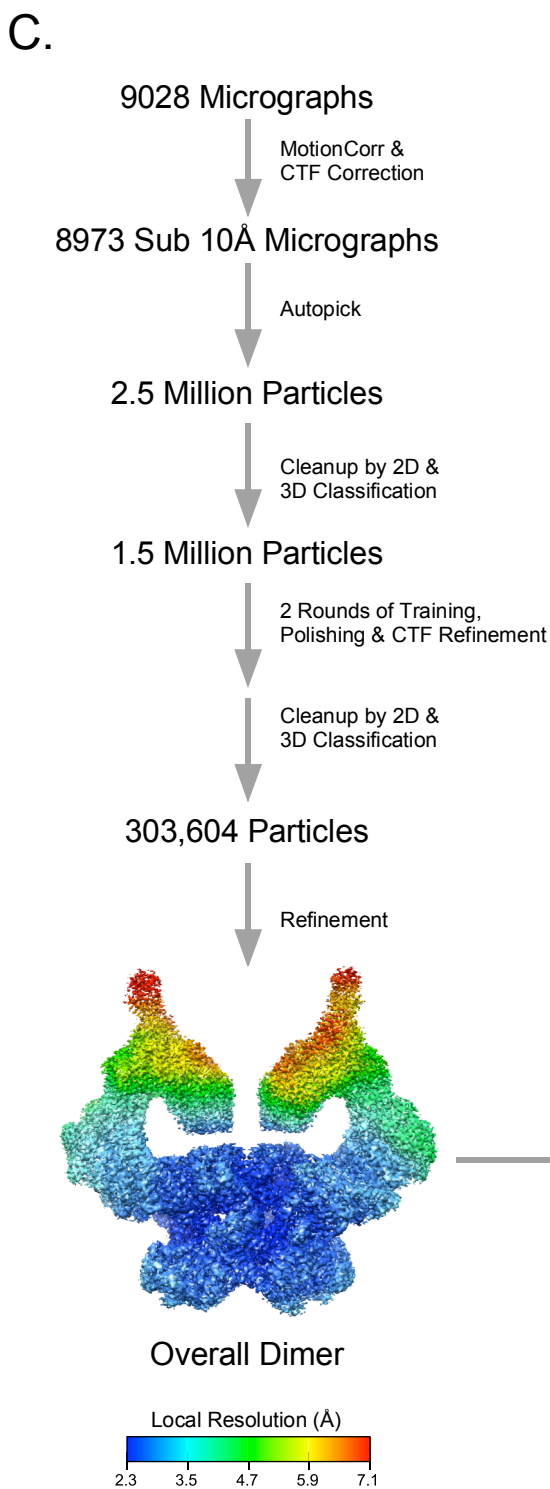
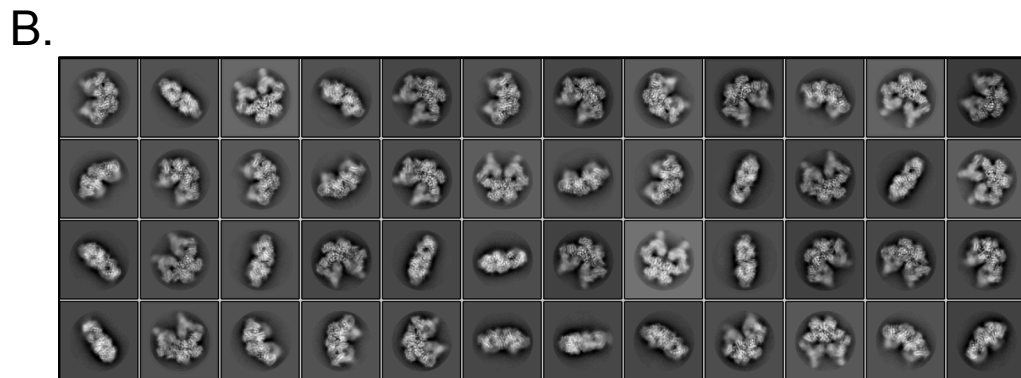
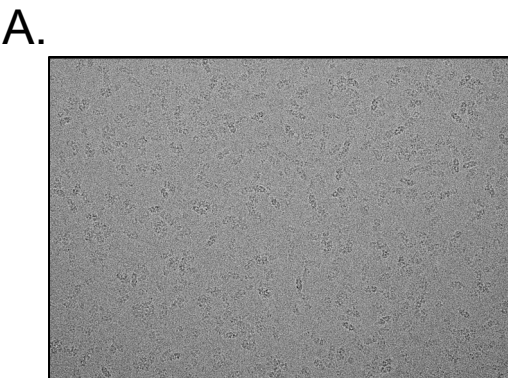


A.

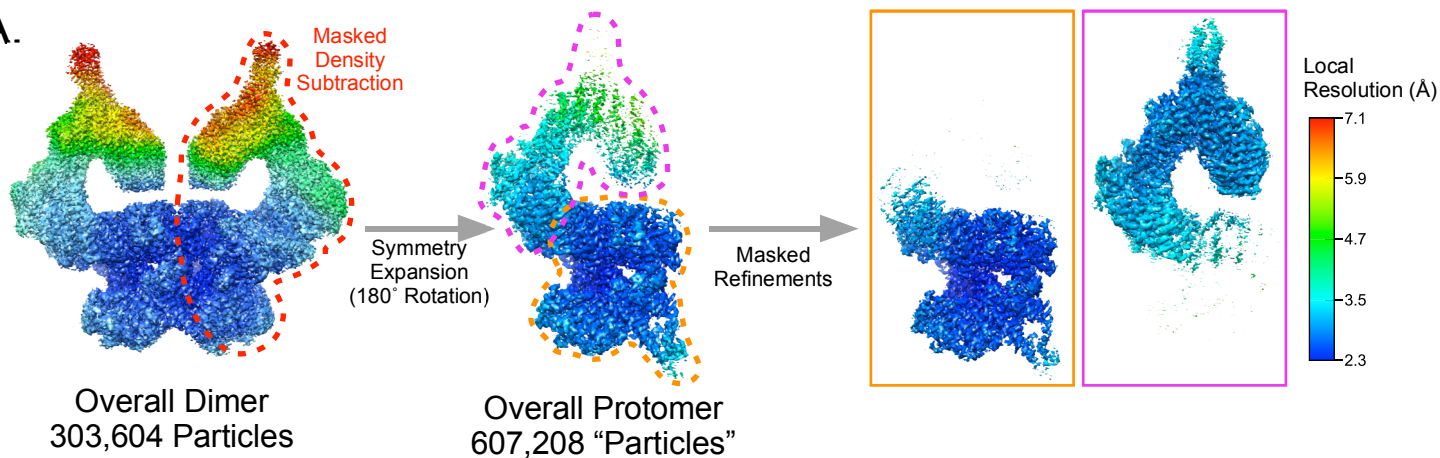


B.



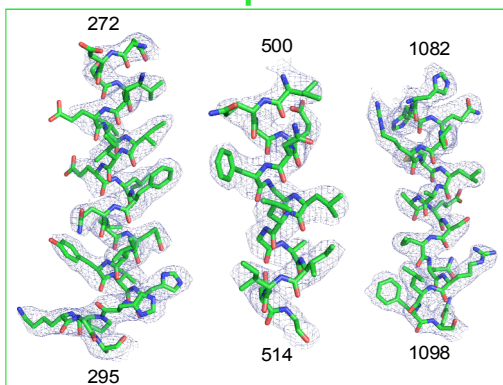


A.

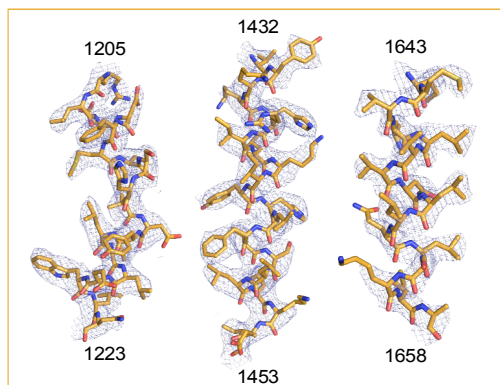


B.

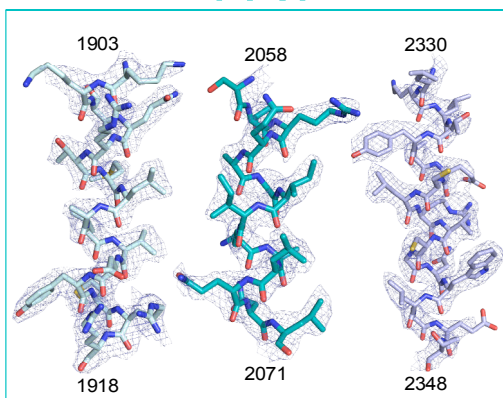
Spiral



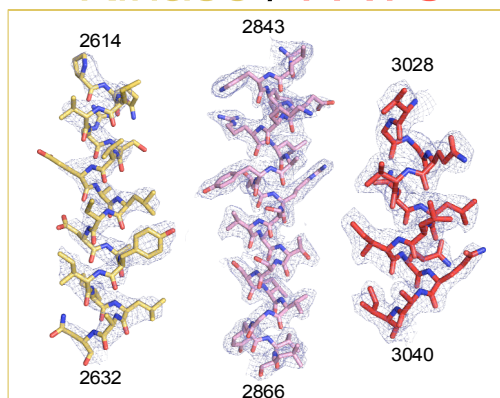
Pincer



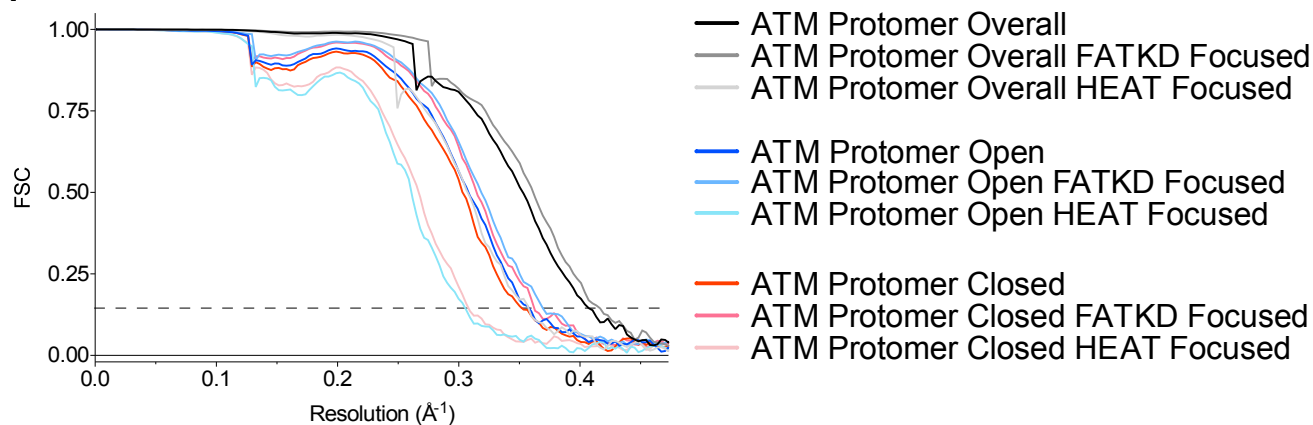
FAT

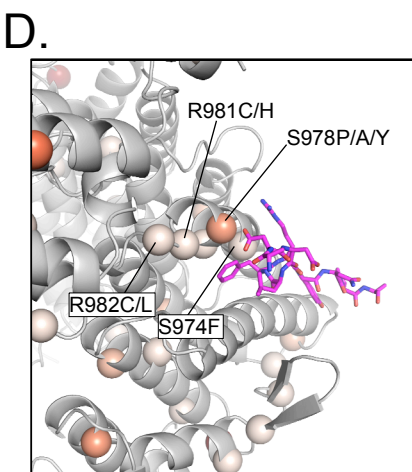
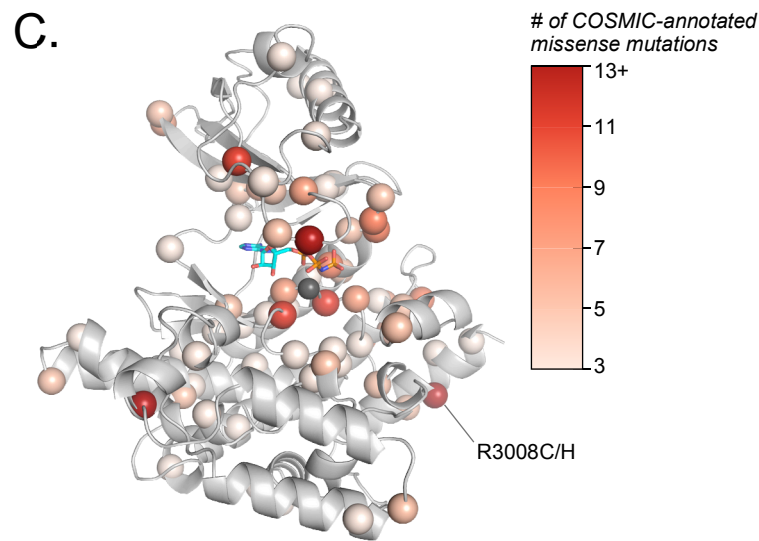
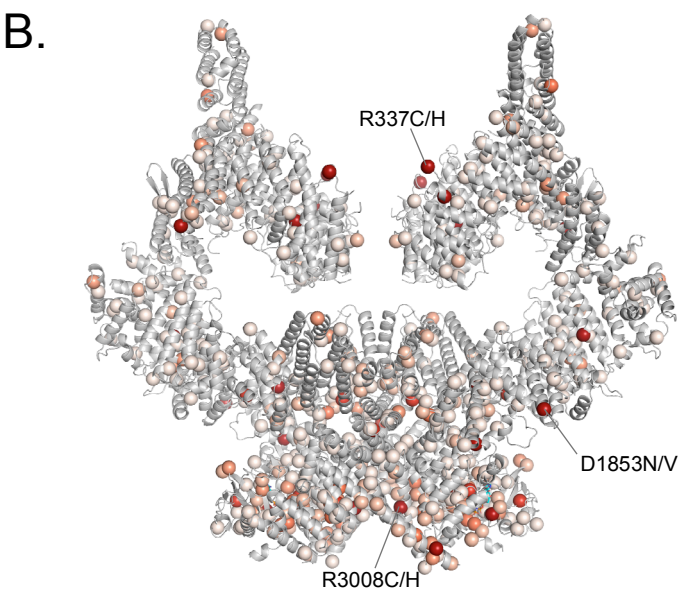
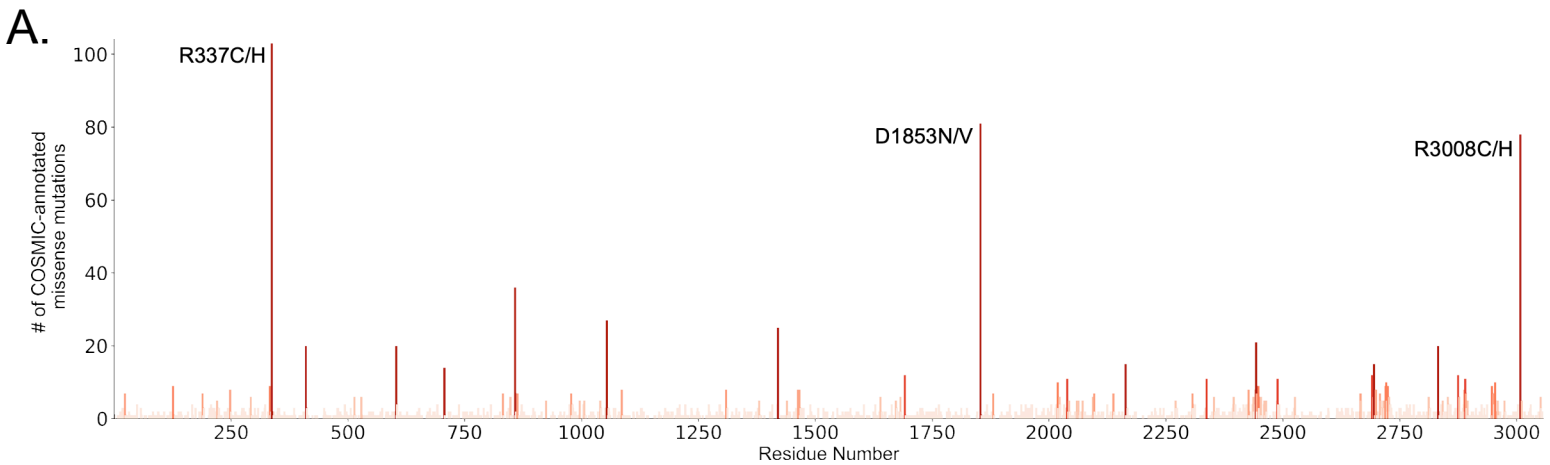


Kinase / FATC



C.



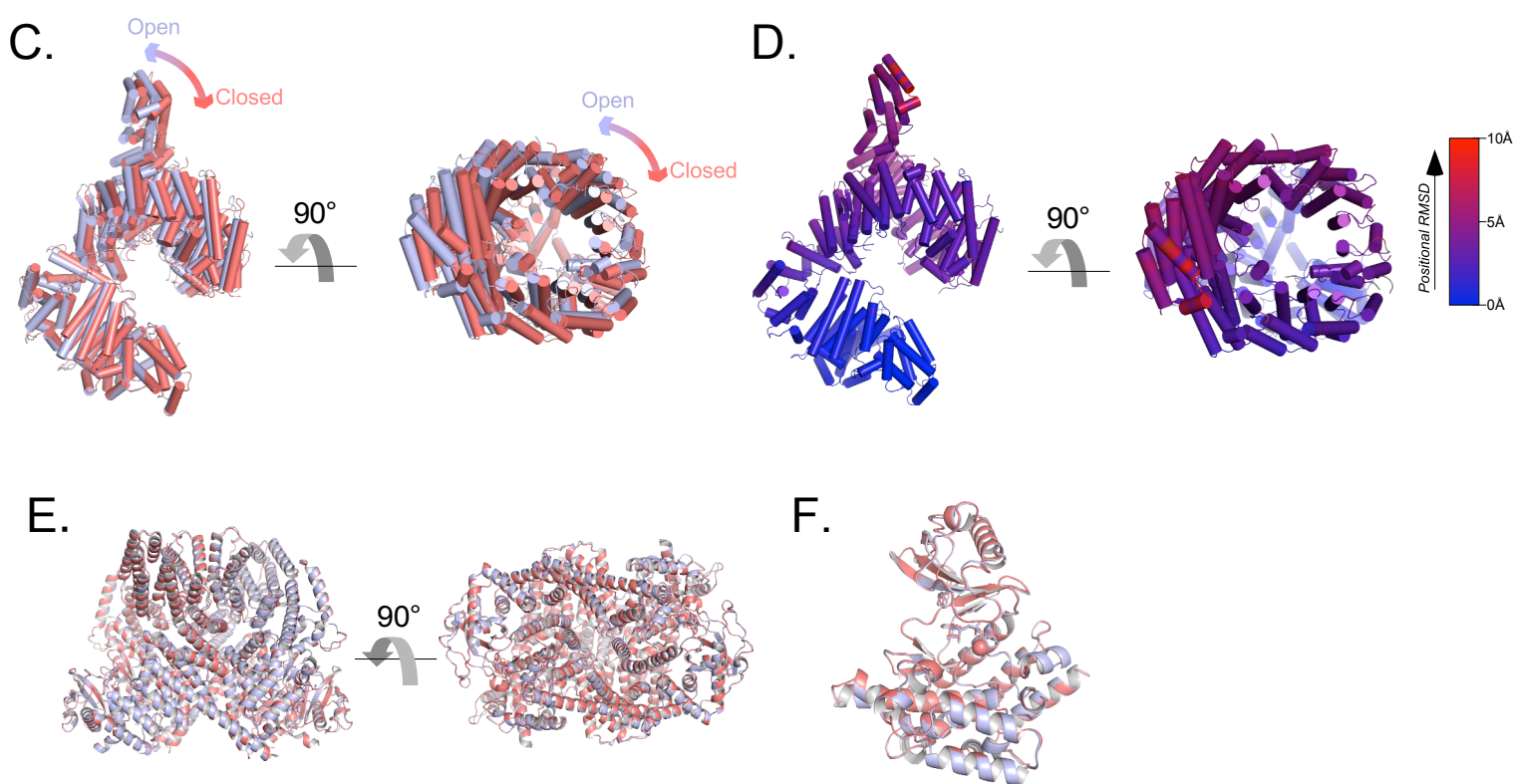
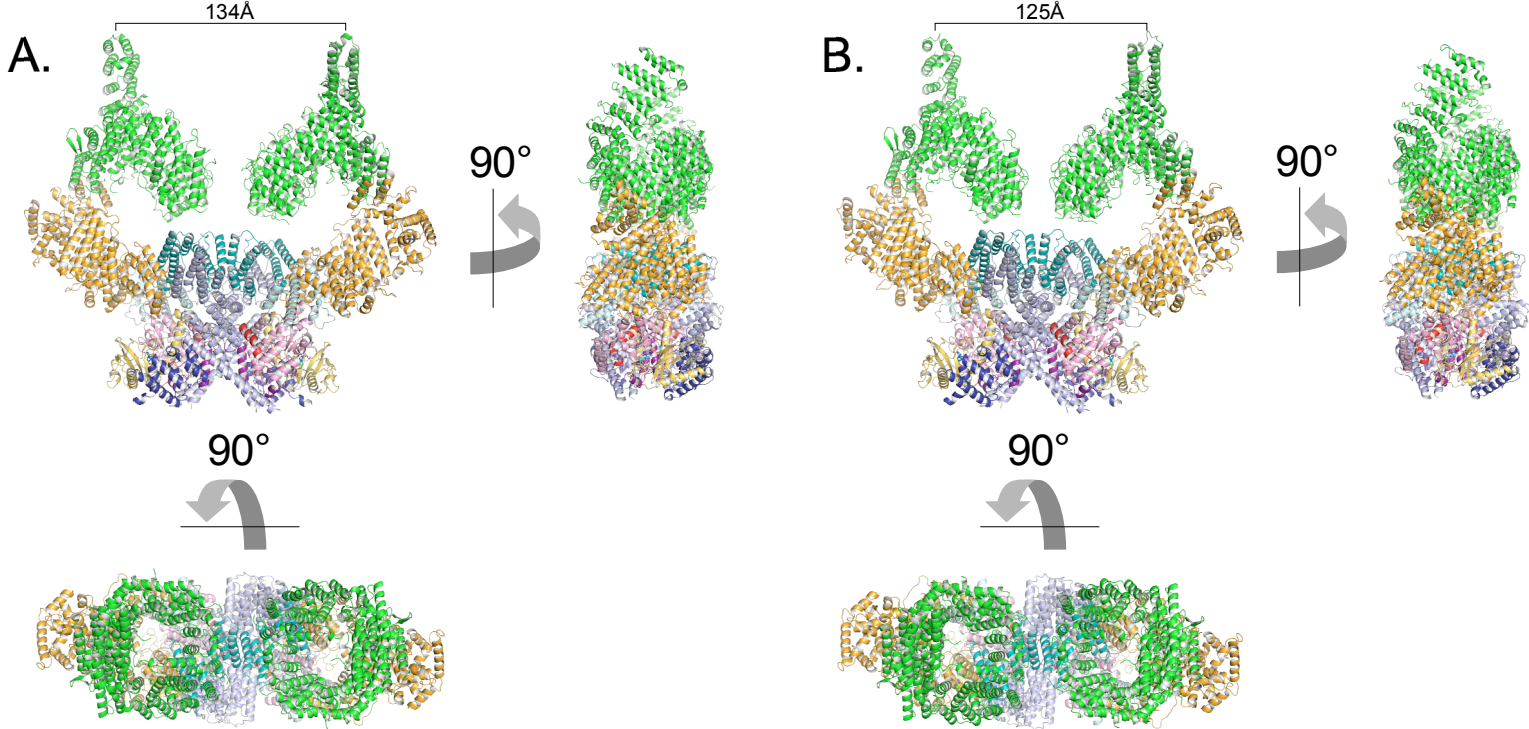


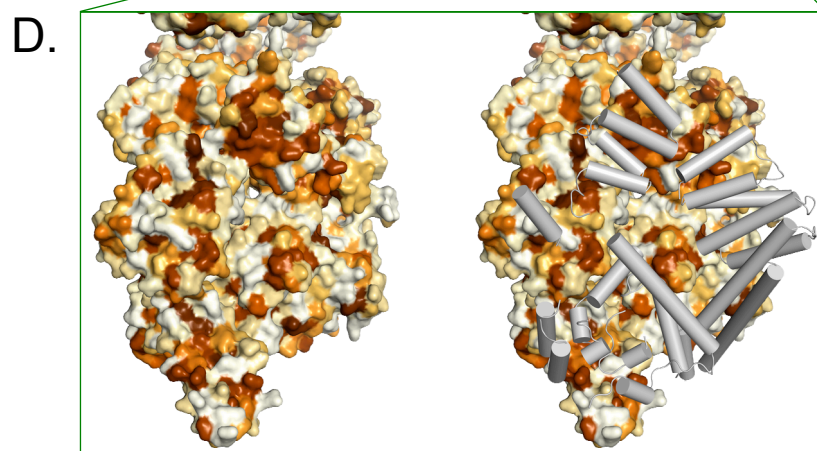
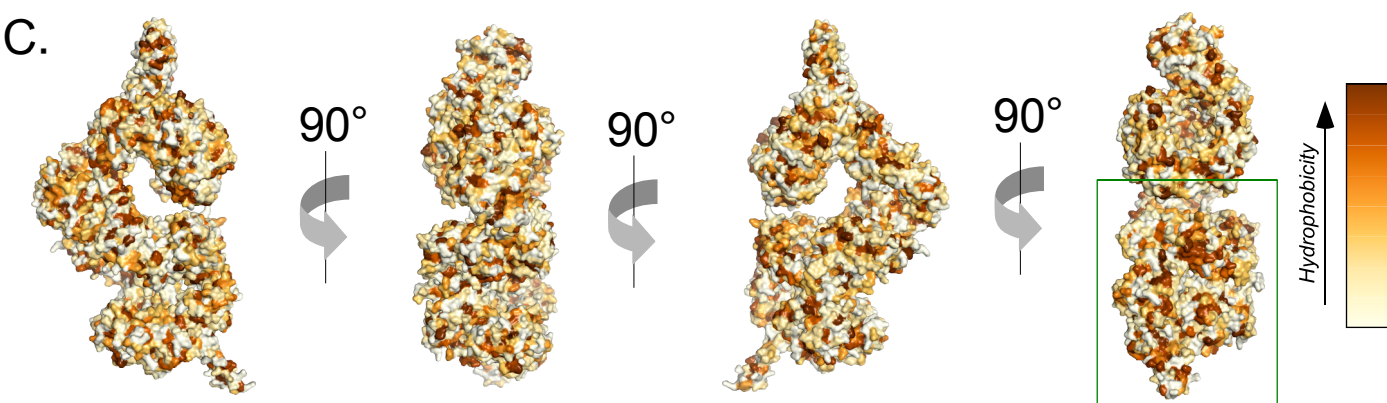
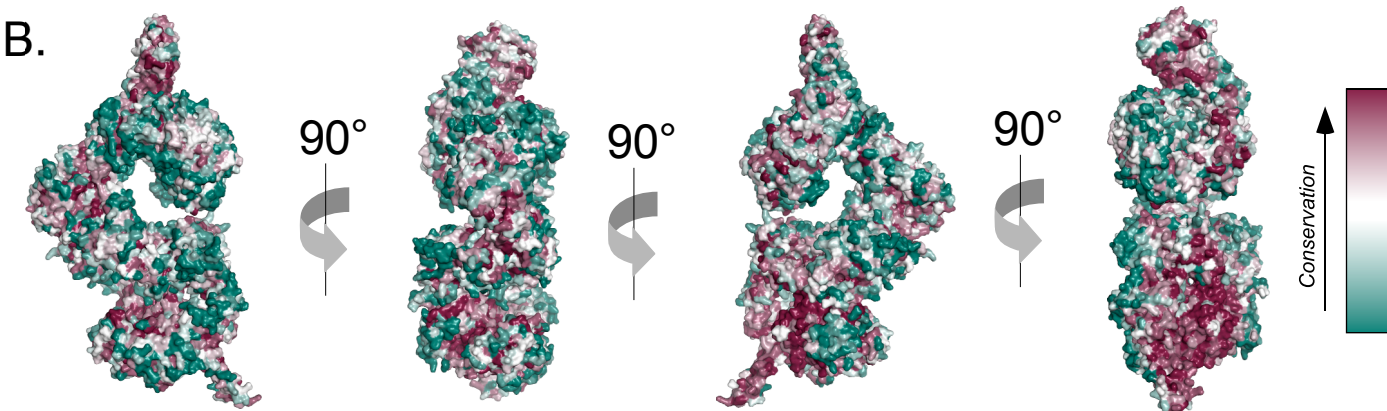
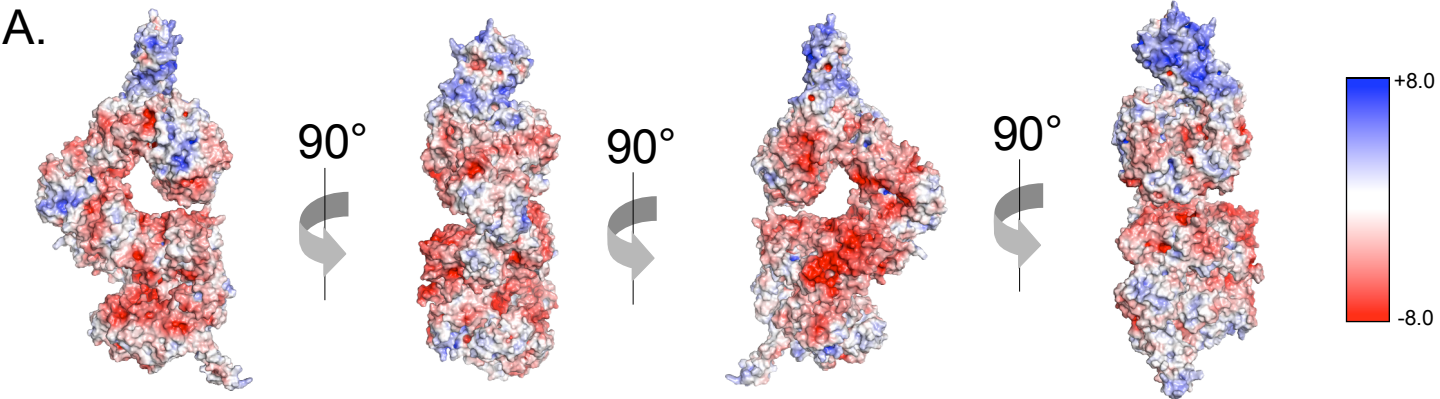
E.

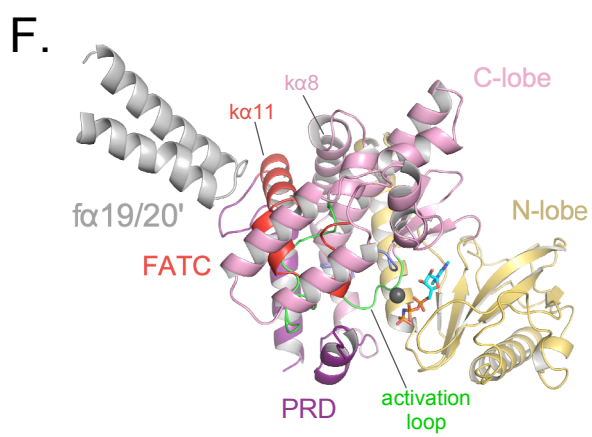
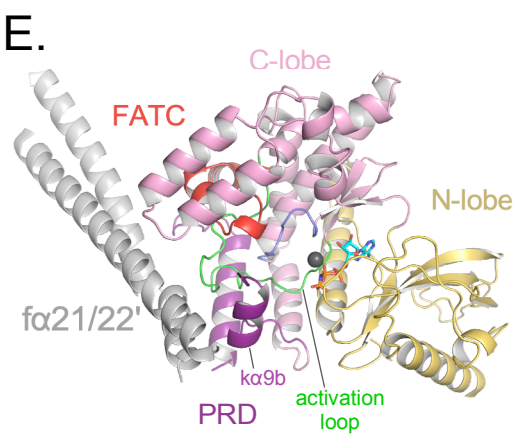
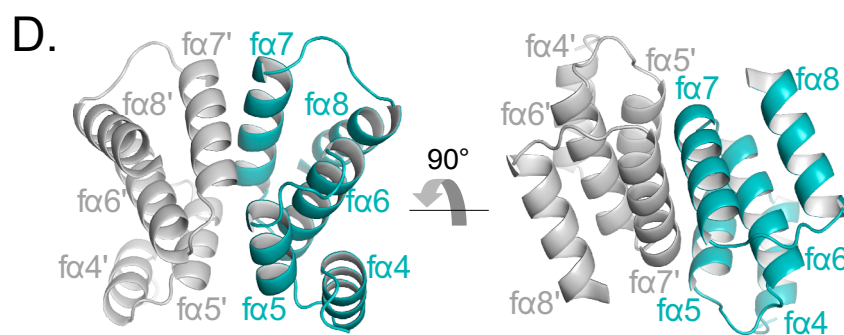
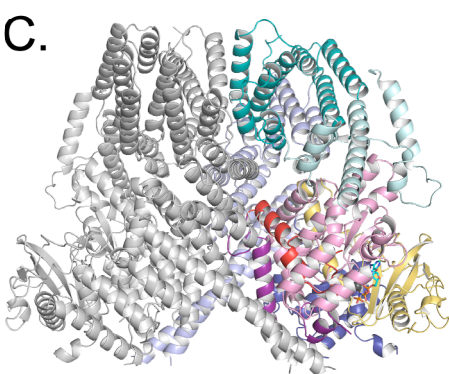
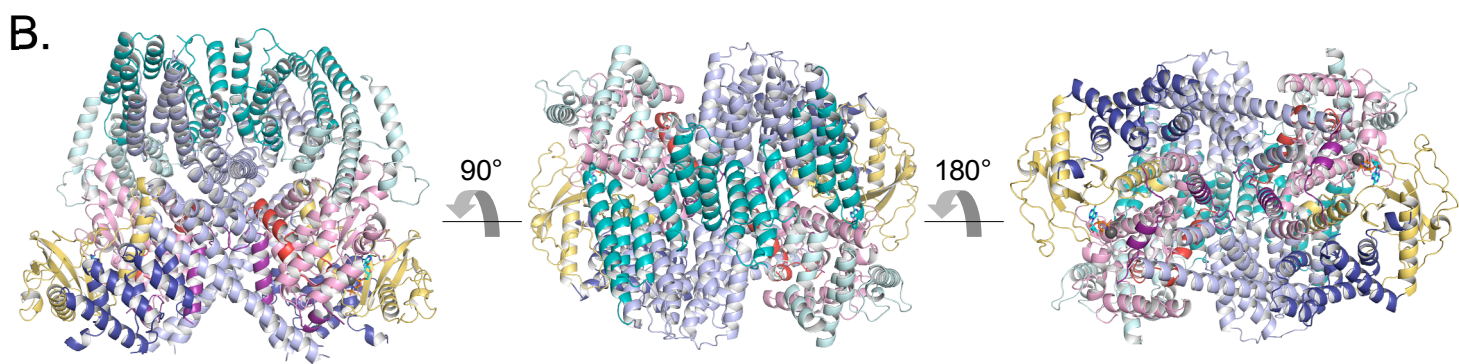
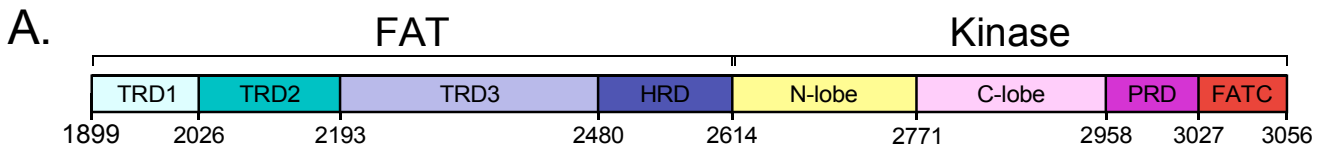
ATM Mutation	COSMIC Frequency	Tissue(s)
S974F	4	Large Intestine Endometrium Biliary Tract
S978P	4	Haematopoietic and lymphoid Breast Prostate
S978A	1	Endometrium
S978Y	2	Large Intestine Endometrium
R981C	3	Haematopoietic and lymphoid Stomach Large Intestine
R981H	1	Endometrium
R982C	2	Large Intestine Adrenal gland
R982L	1	Large Intestine
C987Y	1	Biliary Tract
C987W	1	Haematopoietic and lymphoid
T1020A	1	Large Intestine
V1021L	1	Endometrium
A1024T	1	Large Intestine
F1025S	1	Pancreas
F1025L	1	Haematopoietic and lymphoid
L1028V	1	Lung

F.

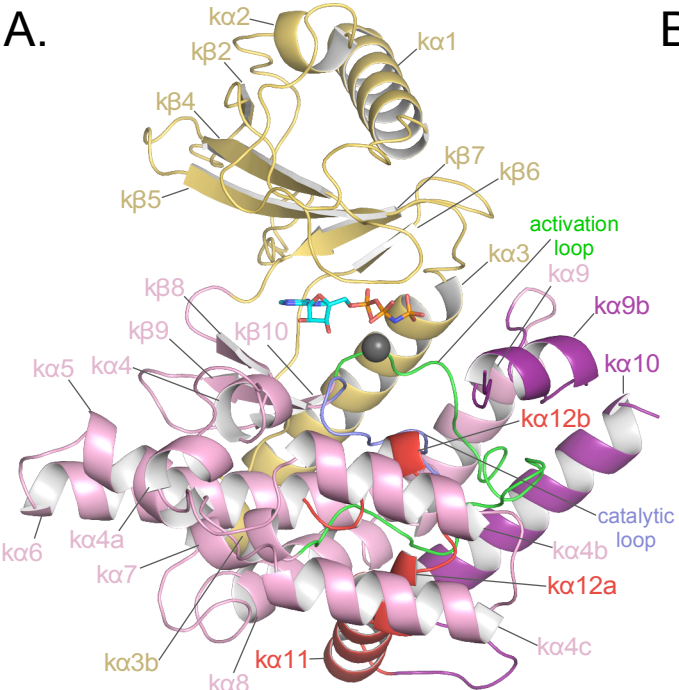
Nbs1 Mutation	COSMIC Frequency	Tissue
Q732K	3	Prostate
E736G	1	Head & Neck
E737K	1	Lung
E737Q	1	Urinary Tract
L739P	1	Large Intestine
A740V	1	Endometrium
D742V	1	Stomach
F744L	1	Endometrium



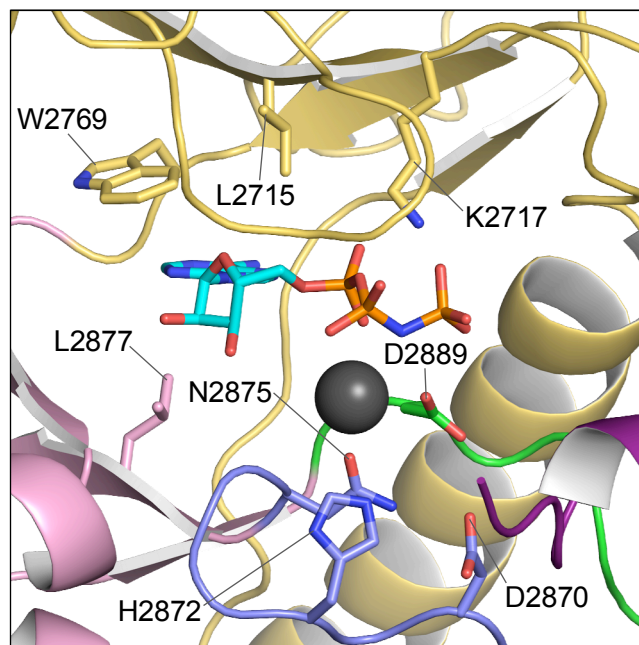




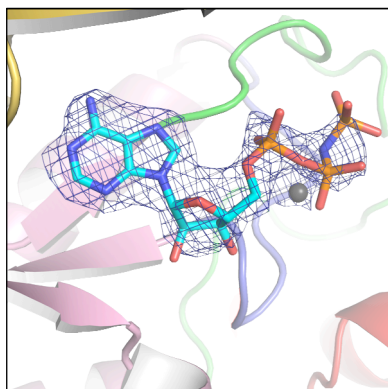
A.



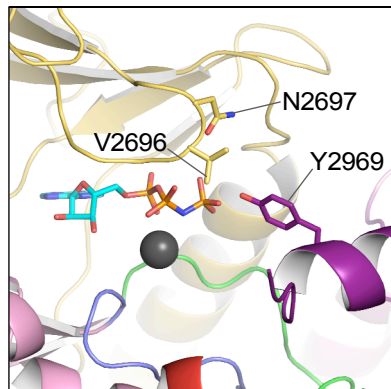
B.



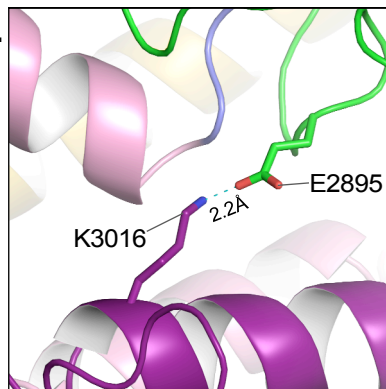
C.



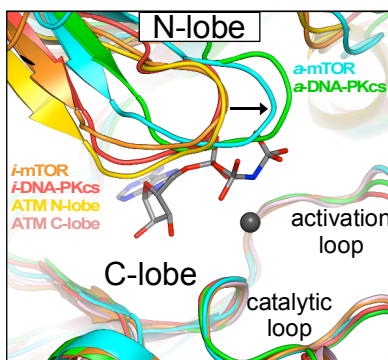
D.



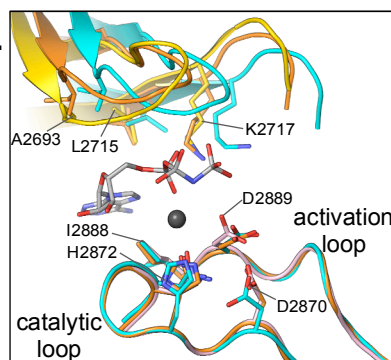
E.



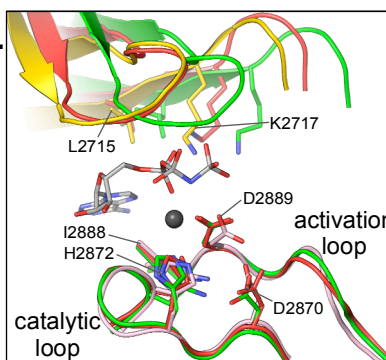
F.



G.

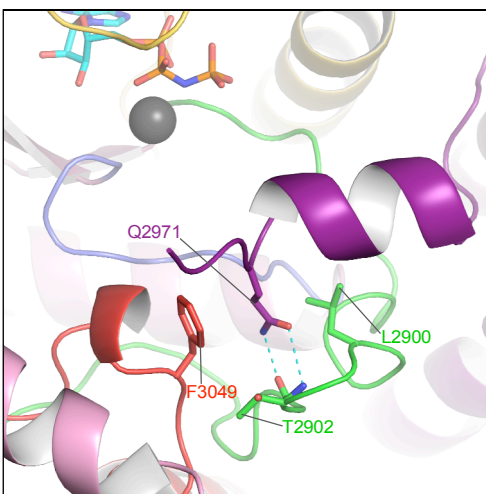


H.



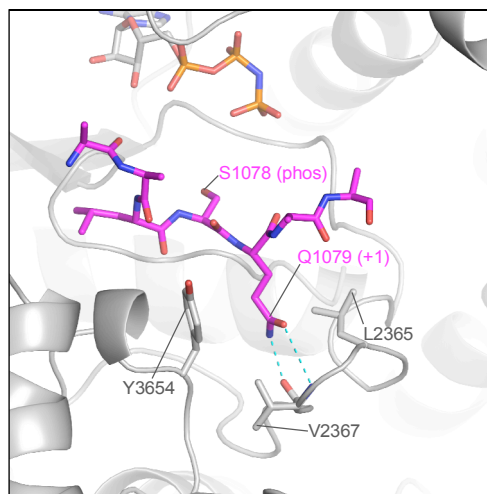
A.

ATM



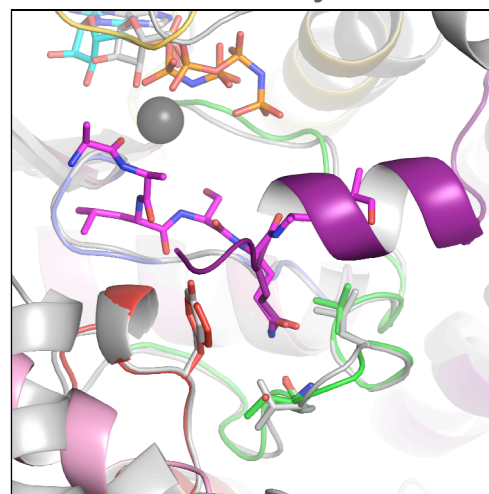
B.

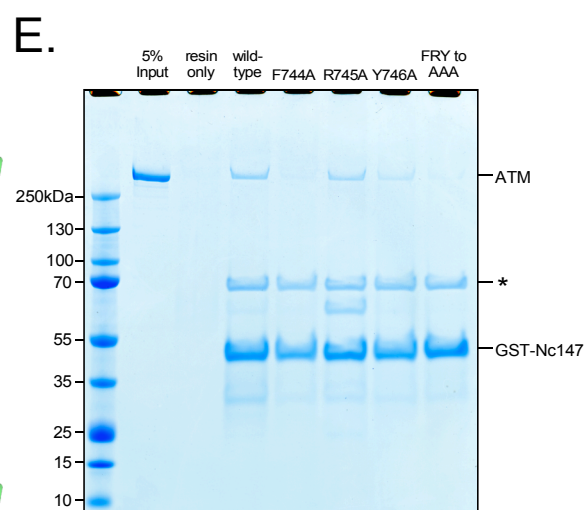
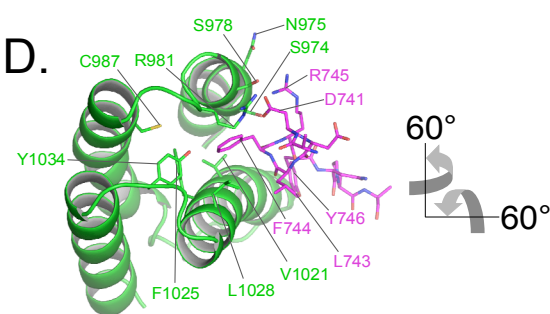
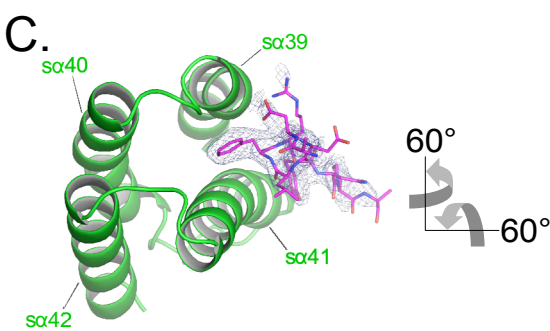
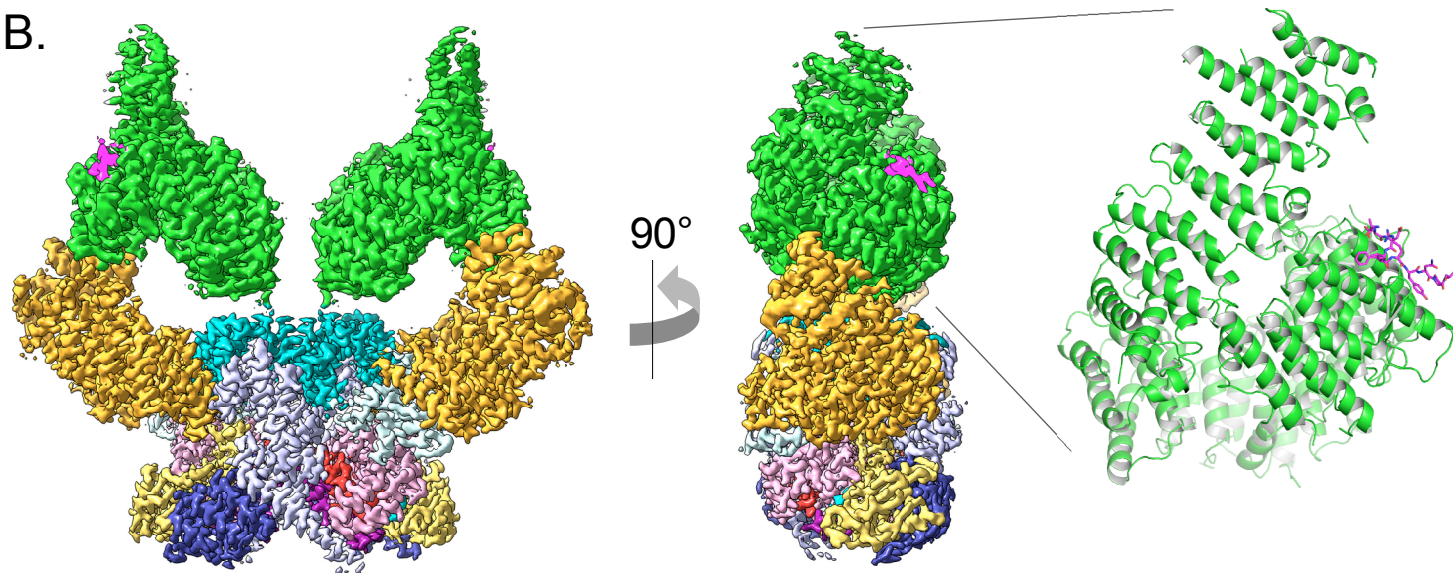
SMG1-UPF1



C.

Overlay

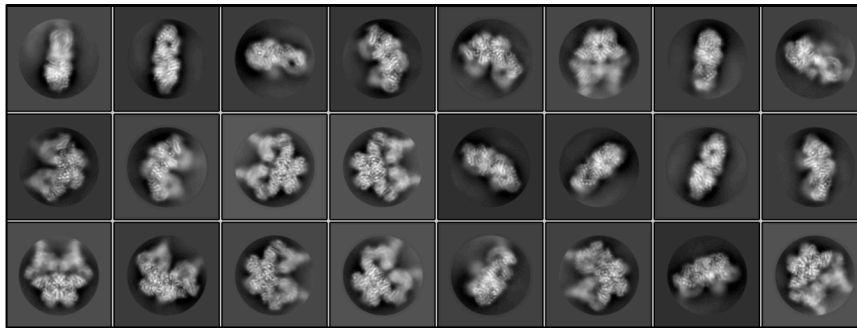




A.



B.



C. 7866 Micrographs

MotionCorr &
CTF Correction

6531 Sub 5Å Micrographs

Autopick

2 Million Particles

Cleanup by 2D &
3D Classification

287,615 Particles

2 Rounds of Training,
Polishing & CTF Refinement

Refinement

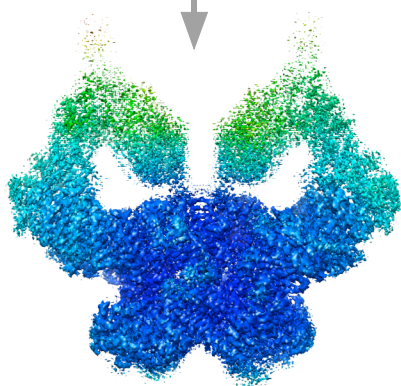
Partial Signal Subtraction &
Symmetry Expansion

575,230 Particles

Focused 3D Classification:
Enrich for Peptide-Bound Particles

481,066 Particles

De-duplicate and Refine

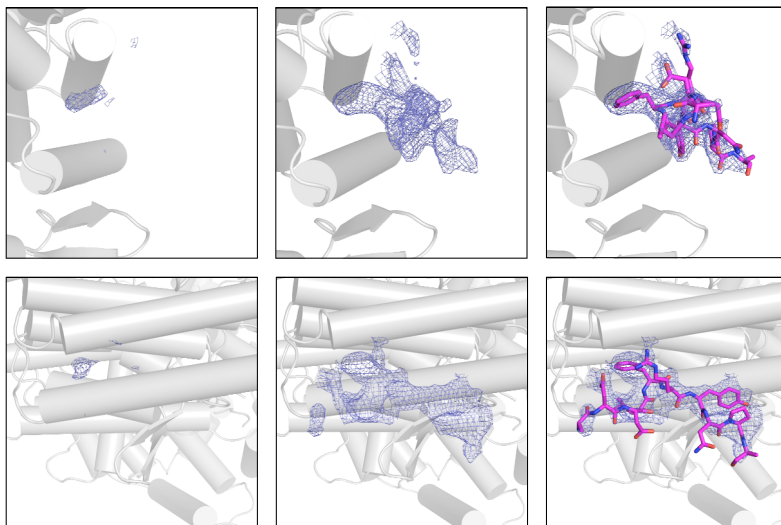


D.

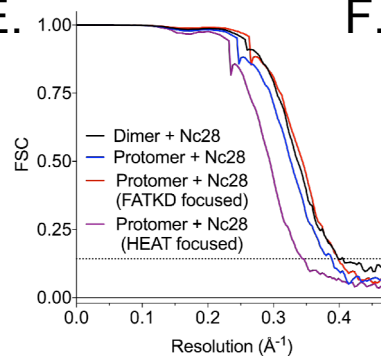
Unbound

+Nc28

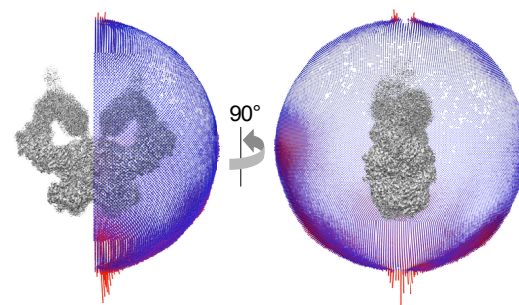
+Nc28 built



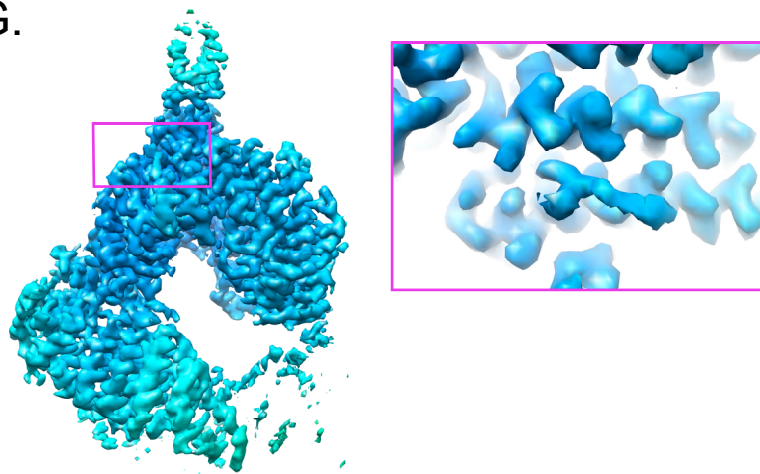
E.

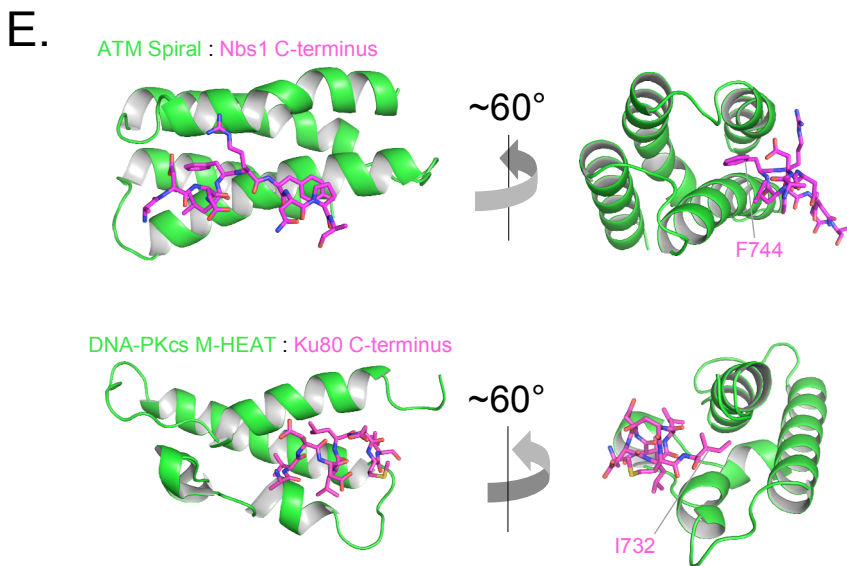
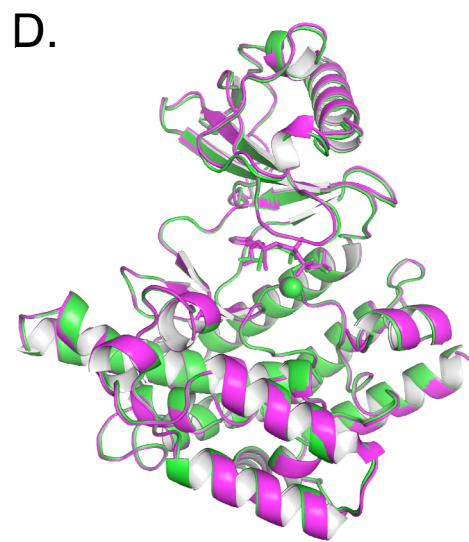
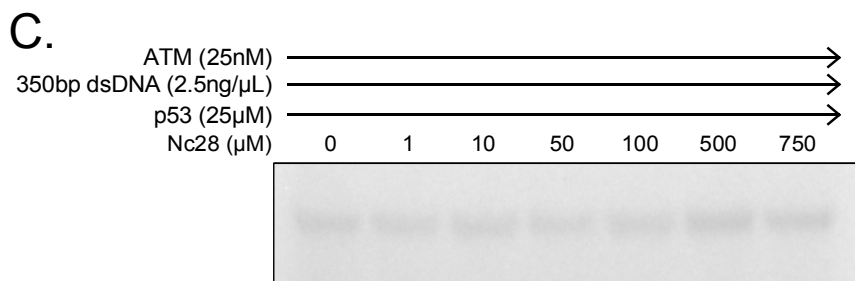
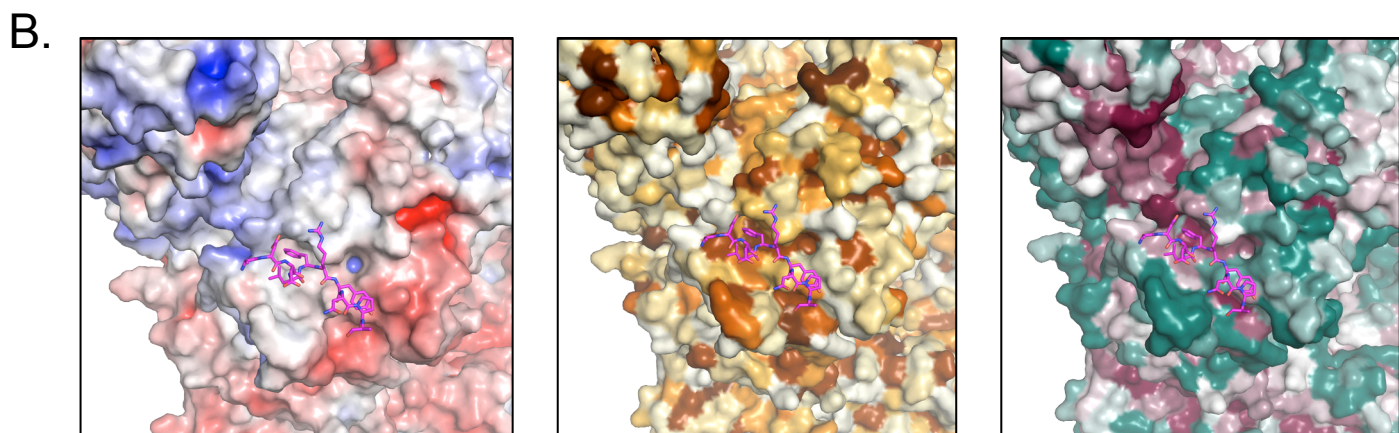
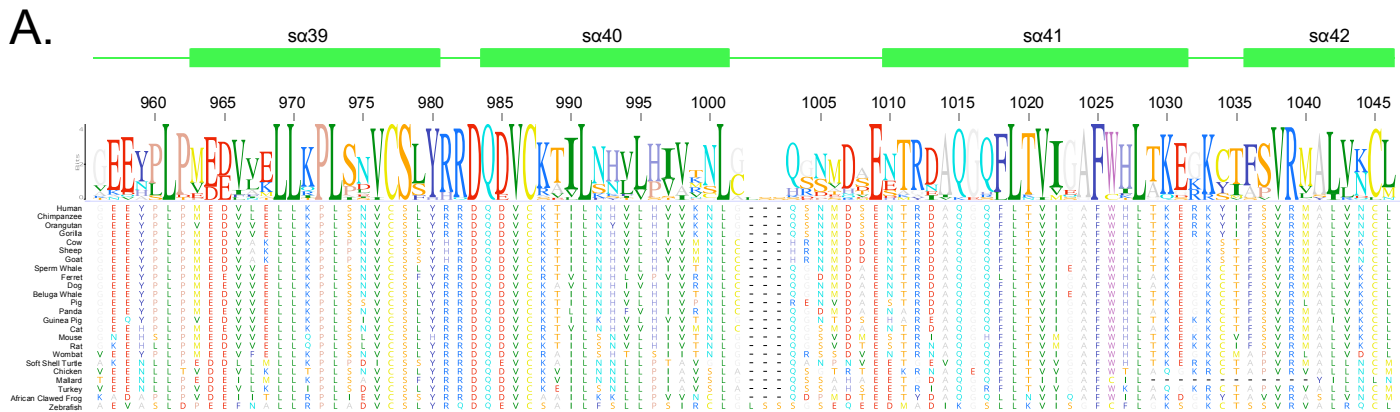


F.

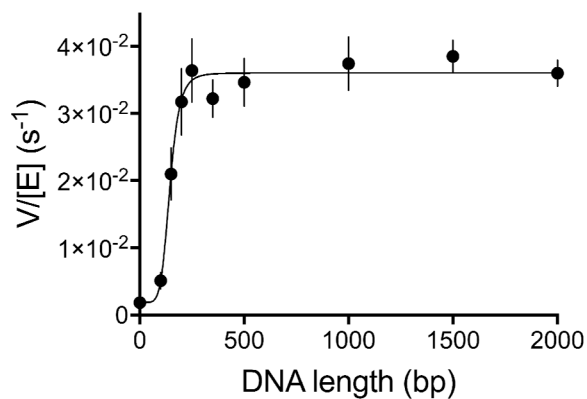
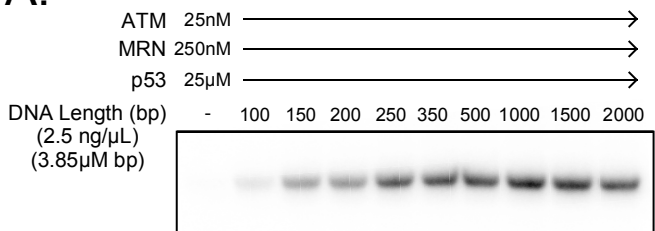


G.

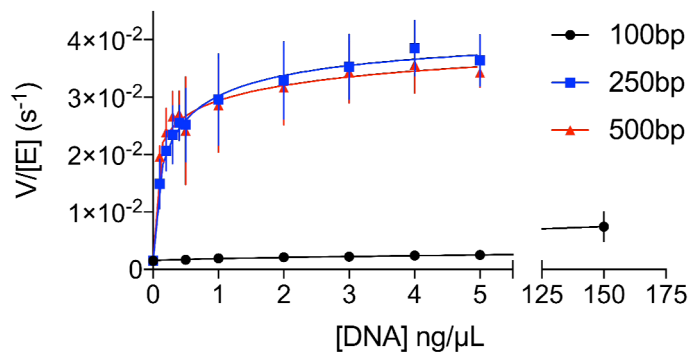
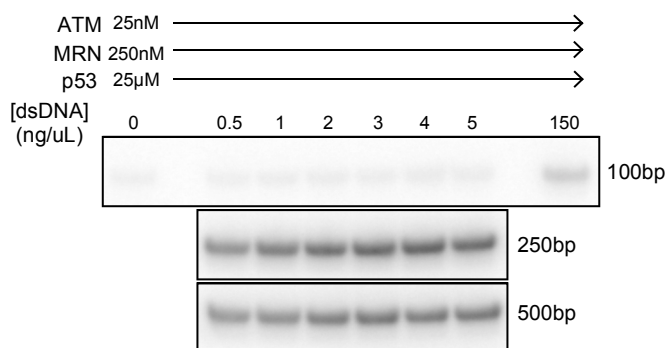




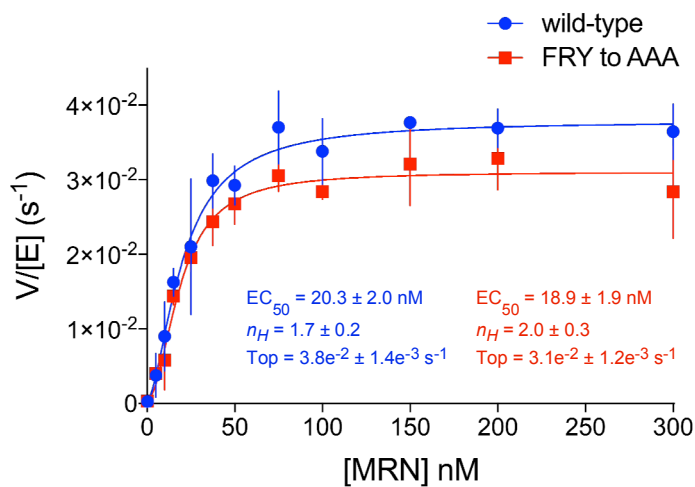
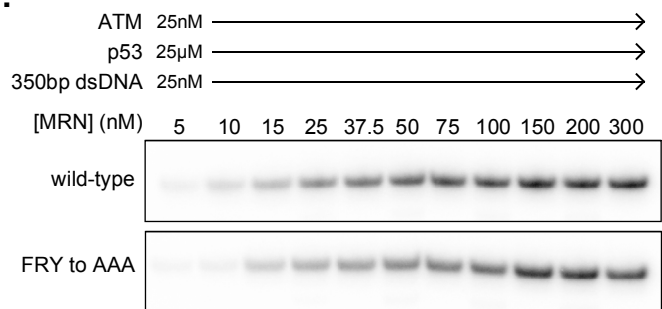
A.

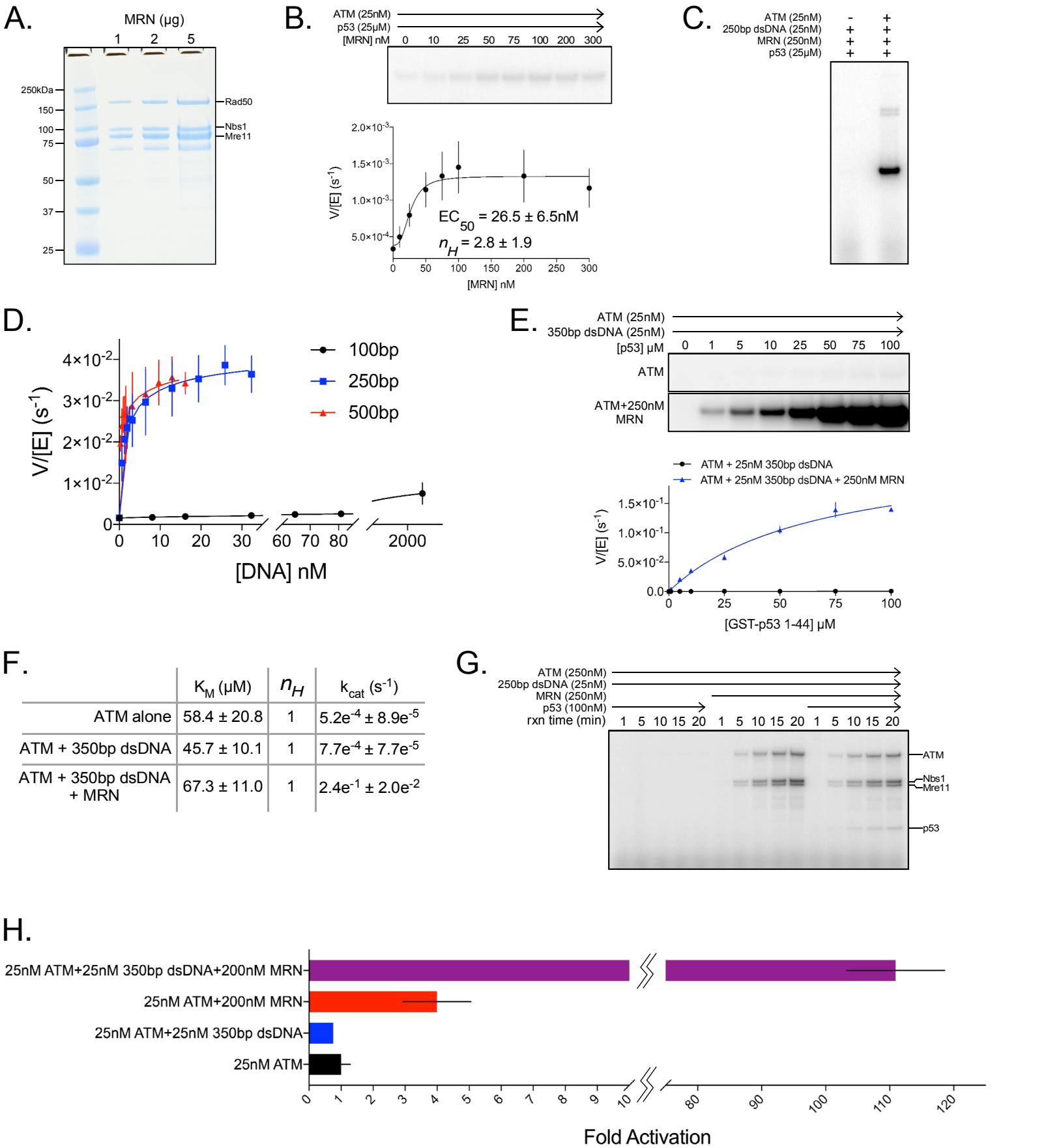


B.

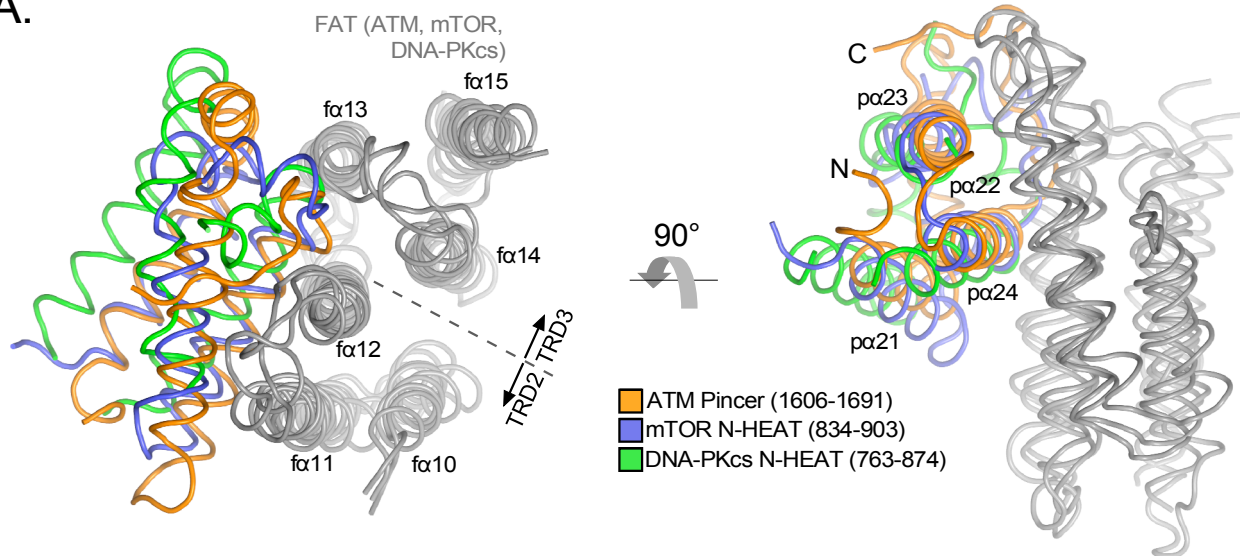


C.





A.



B.

